POLITECNICO DI BARI

Dipartimento di Ingegneria Civile, Ambientale, del Territorio, Edile e di Chimica – DICATECh

CORSO DI LAUREA MAGISTRALE IN INGEGNERIA PER L'AMBIENTE E IL TERRITORIO

Anno Accademico 2020-2021

TESI DI LAUREA IN

An OBIA approach for mapping plastic greenhouses in the Bari area using Deimos-2 and Sentinel-2 satellite images

Relatori: Prof. Eufemia Tarantino; Prof. Manuel Angel Aguilar

Laureando: Claudio Ladisa

Summary

1 Introduction

1.1 Object based image analysis for remote sensing

Environmental monitoring requirements, conservation objectives, the application of spatial planning or ecosystem-oriented management of natural resources, to name a few factors, give considerable urgency to the development of operational solutions capable of extracting tangible information from remote sensing data. Remote sensing images need to be converted into tangible information that can be used in conjunction with other data sets, often within widely used geographic information systems (GIS). As long as the pixel dimensions have typically remained coarser or, at best, similar in size to the objects of interest, emphasis has been placed on per-pixel analysis or even sub-pixel analysis for this conversion, but with increasing spatial resolutions alternative paths have been followed, aimed at obtaining objects made up of more pixels. Object-based methods aim to delineate objects that are readily usable by images, while at the same time combining image processing and GIS capabilities to use spectral and contextual information in an integrative way. In the 2000s GIS and image processing began to grow together rapidly through object-based image analysis (OBIA - or GEOBIA for geospatial object-based image analysis). In contrast to typical Landsat resolutions, high resolution images support different scales within their images. Through a comprehensive literature review, several thousand abstracts were screened and more than 820 OBIA-related articles were analyzed in detail comprising 145 journal articles, 84 book chapters and nearly 600 conference articles. It becomes evident that the early years of OBIA / GEOBIA developments were characterized by the dominance of "gray" literature, but that the number of peer-reviewed journal articles has increased considerably over the past four to five years. The pixel paradigm is starting to show cracks and OBIA methods are making significant progress towards a spatially explicit information extraction workflow, as is required for spatial planning and many monitoring programs. It should be clearly stated that much of the work referred to as OBIA originated around software known as "eCognition. Furthermore, very few "early" OBIA developers used the term "object-based". Some authors have used the “object oriented” (T. Blaschke, 2000), (U.C. Benz, 2004) and some of these subsequently switched to' object-based '(with or without hyphen), while some authors still use "object-based" objects (Navulur, 2007). So far it has been assumed that most authors prefer to use the term" based "as" oriented "may be too closely related to the object oriented programming paradigm. The idea of incorporating contextual information into the classification of remote sensing images can be traced back to the 1970s (R. Kettig D. L., 1976), although the importance of embedding texture increases with increasing resolution. One of the goals of grouping pixels into image objects is to overcome the so-called “salt and pepper effect”. Many researchers have stated that OBIA methods are suitable for overcoming this situation, for example "Thanks to recent improvements in image segmentation, object-based approaches can be used to efficiently delineate and classify land cover (R. Kettig D. L., 2008). It has even been stated in recent articles that "object-oriented processing techniques are becoming more popular than traditional pixel-based image analysis" (R. Kettig D. L., 2009). The “workhorses” of satellite data generation, such as Landsat and SPOT satellites or ASTER and MODIS instruments, have become important in global and regional studies on biodiversity, nature conservation, food security, impact deforestation, desertification monitoring and other fields applications. With the increasing spatial resolution of the 1-m generation of IKONOS (launched in 1999), the sensors QuickBird (2001) or OrbView (2003), new fields of application that had previously been the domain of aerial remote sensing could be addressed by the satellite remote sensing. At the end of 2007, the first commercial satellite with a resolution of less than half a meter (Worldview-1; 0.44m panchromatic) became operational, and we currently see security applications, vehicle detection and many urban applications developing rapidly, in terms both in number and in refinement. For simplification and generalization we can distinguish two main trends: (a) an increasing amount of data produced in an ever wider range of spatial, spectral, radiometric and temporal resolutions, including the high spatial resolutions mentioned above, and (b) programs and systems supranationals orchestrated for regular or on-demand surveys of the earth's surface (e.g. GEOSS, GMES).

1.1.1 Segmentation technique

Before OBIA, the main task of image segmentation was to produce a set of non-overlapping segments (polygons) and this step was completely separate from classification. The problem, however, is the scale: the scale is a "window of perception" (Marceau, 1999) and we typically end up having different scales in the images, if the spatial resolution is finer than the size of the objects of interest. A segmentation algorithm is used in the expectation that it divides the image into (a) relatively homogeneous and (b) semantically significant pixel groups. (D. Marceau, 2003) called these groups "candidate objects" which must be recognized by further processing steps and transferred into meaningful objects. For a high-resolution aerial image, for example, at coarse scales we can discriminate fields or woods, while at finer scales we can discriminate individual trees or plants: the parameters and thresholds in a typical single-scale segmentation algorithm must therefore be tune into the correct scale for analysis. Segments are regions generated by one or more homogeneity criteria in one or more dimensions (of a feature space) respectively. Therefore the segments have additional spectral information with respect to the individual pixels (e.g. average values per band, and also median values, minimum and maximum values, average ratios, variance, etc.), but of even greater advantage with respect to the diversification of the descriptions of the spectral values of objects is the additional spatial information for the objects. It has often been stated that this spatial dimension (distances, proximity, topologies, etc.) is crucial for OBIA methods and that this is one of the main reasons for the marked increase in the use of segmentation-based methods in recent times, compared to the use of image segmentation in remote sensing during the 1980s and 1990s. Figure 1 schematically shows the relationship between the spatial resolution and the object under examination. Although we have difficulty defining generically applicable thresholds, we can semantically differentiate between these three situations. For simplicity, we can consider the pixel in a similar way to the spatial resolution. Furthermore, when considering Shannon's sampling theorem (sometimes called Nyquist - Shannon's sampling theorem), we can conclude that an object should be on the order of one-tenth the size of the sampling pattern, the pixel, to ensure that be completely independent of its random position and orientation with respect to the sampling scheme. The three situations graphically outlined in Figure 1 require completely different techniques for unraveling the information from the datasets. It can be assumed that situations (a) and (b) leave little choice when the task is to identify, classify and characterize a given object as illustrated. Situation (c), however, can be considered a "high resolution situation"' and only here can the specific advantages of the OBIA approach be used, although regionalization approaches have also been applied to other situations, for example Landsat images, and recent studies have also used OBIA methods for medium or coarse resolution data.

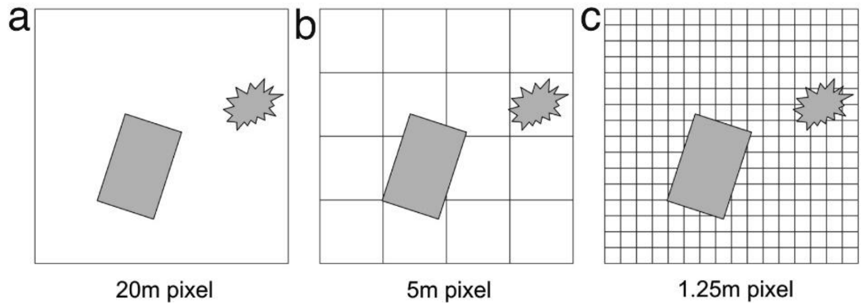

(Fig. 1 - Relationship between the objects considered and spatial resolution: (a) low resolution: pixels significantly larger than the objects, sub-pixel techniques required. (b) medium resolution: pixel and object sizes are of the same order, pixel by pixel techniques are appropriate. (c) high resolution: pixels are significantly smaller than objects, pixel regionalization into pixel groups is required and finally objects)

1.1.2 Remaining problems

All studies and publications have demonstrated the potential of OBIA but also reveal that other more specific problems can arise for high resolution situations. In high resolution images, for example, each pixel is not strictly related to the physiognomy of the vegetation as a whole and the vegetation always shows heterogeneity as a result of irregular shadows or shadows. However, many studies are able to show that the advantage of being able to aggregate pixels to segments of objects and to address the characteristics of objects through sub-objects allows to explicitly deal with various types of heterogeneity within the patch, which allows applications in the study of forest gaps, vegetation irregularities or landscape complexity. It is widely recognized that advances in sensor technologies, particularly those related to the spatial resolution of sensors, are helping to make remote sensing more appropriate for detailed studies of the Earth's surface. The resulting massive amounts of data present a challenge, and object-based methods are not the only way to address this problem. Developments in image classification techniques, notably artificial neural networks (ANNs), fuzzy set methods, genetic algorithms, and support vector machines, to name a few, may offer the prospect of a better representation of complex environments. One of the most recent trends is that OBIA methods become part of dedicated workflows and converge with leading GIS applications. This rapidly growing body of scientific literature conveys a sense of optimism that OBIA methods generate geospatial information on multiple scales, mitigated by a certain concern that classification rules and increasingly complex workflows raise at least as many research questions as they solve it.

1.1.3 OBIA approach perspective

One of the most recent trends is that OBIA methods become part of dedicated workflows and converge with leading GIS applications. This rapidly growing body of scientific literature conveys a sense of optimism that OBIA methods generate geospatial information on multiple scales, mitigated by a certain concern that classification rules and increasingly complex workflows raise at least as many research questions as they solve it. It is recognized that the higher resolution and detection detail available using improved optical instruments, Radar, LiDAR or even Sonar create problems with the "traditional" approach to land use / land cover mapping. OBIA supports attempts to overcome the centric view of land cover, which is limited to a purely descriptive categorization of the spectral characteristics of pixels, and paves the way for a combined use of spectral and spatial (contextual) information towards the development of “and use”. The OBIA approach to detect PCG and PMF is much more recent than PB analysis. Tarantino and Figorito (Tarantino & Figorito, 2012) published the first work based on OBIA to map plastic-covered vineyards from true color aerial data in Southern Italy. Novelli (Novelli, Nemmaoui, & Aguilar, 2016) carried out the first work based on Sentinel-2A Multispectral Instrument (MSI) and Landsat-8 OLI images to map PCG by adopting an OBIA approach and RF classifier. In this case, the segmentation step was performed on a very high resolution (VHR) image (WV2), thus focusing the classification step on the spectral information provided by Landsat-8 and Sentinel-2A data. (Balcik, Senel, & Goksel, 16–19 July 2019) employed Sentinel-2 images to classify greenhouses in Turkey, demonstrating the valuable contribution of the PGI index proposed in (Yang, et al., 2017). It is necessary to highlight that the OBIA approach has usually performed better than the PB approach, even working on medium resolution satellite imagery such as Landsat-8 OLI.

1.2 OBIA approach in the Sentinel-GH project

1.2.1 Development of agricultural activity under plastic

The practice of under plastic agriculture has had a great development in Spain, especially in Almeria, during the past 60 years, assuming a key economic driver in the area. In recent times, this productive sector is being affected by an unstable and changing geopolitical situation of the markets. In this regard, facts like the entry into force of the new agricultural agreement between the European Union (EU) and The Kingdom of Morocco adopted in 2012, or the Russian veto of horticultural products from UE in August, 2014, are causing important changes in the market prices of products grown in greenhouses, which significantly affect farmers and agribusiness. In order to alleviate these changes in market prices, each agricultural cooperative in Almeria is already making a planning acreage that their partners must dedicate to each product. However, a more globalized planning of horticultural productions would be desirable. Certainly, the possibility of knowing the crops are being grown under greenhouse in an agricultural campaign, both at the local productive sector and at the direct competitors, would help decision making and avoid having to destroy tons of horticultural products to keep prices. In recent years and in the framework of the National Research Plan Project referenced as CTM2010-16573, the capabilities of commercial very high resolution (VHR) satellite images to generate highly accurate georeferenced products such as orthophotos, digital surface models (DSMs) or land cover maps by using object based image analysis (OBIA) approaches have been demonstrated. More recently, the results attained from the project AGL2014-56017-R have shown the possibility of improving, not only the classification of greenhouses by using OBIA techniques and time-series of satellite imagery but also the horticultural crops that are growing under plastic coverings. To date, an Overall Accuracy value ranging from 75% to 80% has been achieved in the classification of autumn and spring crops in Almería (Fig. 2), being melon, watermelon, pepper and tomato the crops that showed better results. Against this background, the overall objective of this project in the field of remote sensing is to develop an object-based image analysis (OBIA) methodology to map and classify, exclusively using multi-temporal satellite optical images (WorldView-3, Deimos-2, Landsat 8 and Sentinel-2), horticultural crops grown in greenhouses. In order to study the possible for methodology transfer between greenhouses areas anywhere in the world, in this project we have added three new study areas (Agadir, Morocco; Antalya, Turkey; Bari, Italy) to the existing one located in the sea of plastic (Almería).

(Fig. 2 – "Plastic sea" in Almeria)

1.2.2 Horticultural crop identification

Detection and mapping of greenhouses by remote sensing is a complex task, already addressed in numerous studies. In the research work (Manuel A. Aguilar A. V., 2015), the innovative goal was based on the identification of greenhouse horticultural crops growing under plastic covers in the 2013. For this goal, object-based image analysis (OBIA) and a decision tree classifier (DT) were applied to a set consisting of eight Landsat 8 OLI images collected from May to November 2013. In addition, a single WorldView-2 satellite image acquired on September 30, 2013 (Fig.3) was also used as a source of data. In this approach, basic spectral information, textural features and different vegetation indices (VIs) derived from Landsat 8 and WorldView-2 multitemporal satellite data were calculated on previously segmented image objects in order to identify four of the crops. Most popular fall plants grown in greenhouses in Almería, Spain (i.e. tomato, pepper, cucumber and eggplant). The best classification accuracy (81.3% overall accuracy) was obtained using the full Landsat 8 time series. These results were considered good in the case of tomato and pepper crops, being significantly worse for cucumbers and the eggplants. These results were hardly improved by adding WorldView-2 image information. The most important information for the correct classification of the different crops under greenhouses was related to the management practices of the greenhouse and not to the spectral properties of the crops themselves.

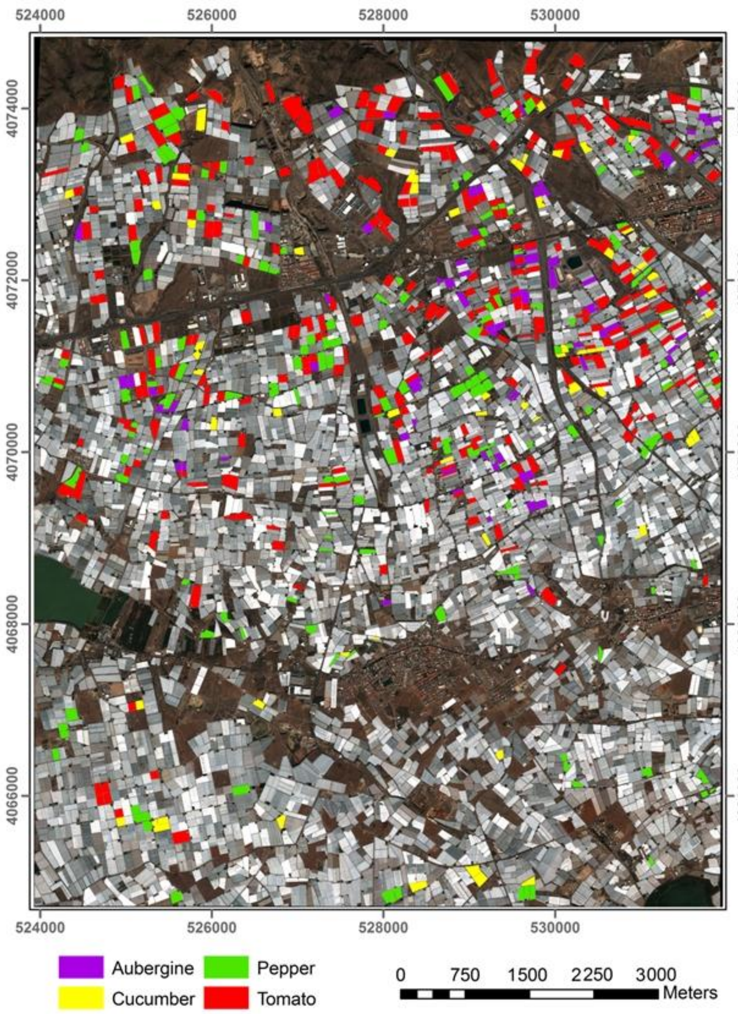

(Fig. 3 – Horticultural crop identification in Almeria)

A few years later in the (Abderrahim Nemmaoui, 2018) article a direct workflow is developed to identify crops growing under plastic covered greenhouses (PCG) and based on multi-temporal and multi-sensor satellite data. This workflow consists of four phases: (i) data preprocessing, (ii) PCG segmentation, (iii) binary pre-classification between greenhouses and non-greenhouses, and (iv) classification of greenhouse horticultural crops for two seasons agronomic (autumn and spring). The segmentation step was performed by applying a multi-resolution segmentation algorithm on the preprocessed WorldView-2 data. The free-access (Eufemia Tarantino, 2017) command line tool was used to determine the most suitable multi-resolution algorithm parameters. Two decision tree models were made which are used on the Plastic Greenhouse index to perform binary classification of greenhouse / non from the Landsat 8 and Sentinel-2A time series, obtaining an overall accuracy of 92.65% and 93.97%, respectively. Regarding the classification of crops in PCG, pepper in autumn and melon and watermelon in spring provided the best results (F_{β} around 84% and 95% respectively). Sentinel-2A time series data showed slightly better accuracies than Landsat 8 data.

1.2.3 Greenhouses mapping

The mapping of greenhouses through remote sensing has received great attention in recent decades. In the paper authored by (Manuel A. Aguilar A. N., 2016)the innovative objective is based on the mapping of greenhouses through the combined use of very high resolution satellite data (WorldView-2) and Landsat 8 Operational Land Imager (OLI) time series in the context of an analysis of the object-based image (OBIA) and the classification of the decision tree. Therefore, WorldView-2 in this case was mainly used to segment the study area by focusing on the individual greenhouses. Basic spectral information, spectral and vegetation indices, textural features, seasonal statistics and a spectral metric (Moment Distance Index, MDI) derived from Landsat 8 time series and / or WorldView-2 images were calculated on previously segmented image objects. To test its temporal stability, the same approach was applied for two different years, 2014 and 2015. In both years, MDI was indicated as the most important feature for surveying greenhouses. Furthermore, the threshold value of this spectral metric was found to be extremely stable for both Landsat 8 and WorldView-

2 images. A simple decision tree has finally been proposed that always uses the same threshold values for the characteristics of the Landsat 8 and WorldView-2 time series. Overall accuracies of 93.0% and 93.3% and kappa coefficients of 0.856 and 0.861 were achieved for the 2014 and 2015 datasets, respectively. In the (Antonio Novelli, 2016) publication, the first comparison between Sentinel-2 (S2) Multi Spectral Instrument (MSI) and Landsat 8 (L8) Operational Land Imager (OLI) data aimed at surveying greenhouses. Two closely related scenes over time, one for each sensor, were classified using Object Based Image Analysis and Random Forest (RF). The RF input consisted of several object-based characteristics calculated from spectral bands and including mean values, spectral indices and textural characteristics. Comparisons of S2 and L8 data were also extended using a common segmentation dataset extracted from VHR World-View 2 (WV2) images to highlight differences only due to their specific spectral contribution. The best combinations of bands to perform segmentation were found through a modified version of the Euclidian Distance 2 index. Four different RF classification schemes were considered, reaching 89.1%, 91.3%, 90.9 respectively. % and 93.4% as the best overall accuracies, evaluated over the entire study area. (Manuel Ángel Aguilar, 2020) reported that the consistency spectrum of the surface reflectance values of the Sentinel-2 MSI (S2 L2A) and Landsat 8 OLI (L8 L2 and the pansharpened and atmospheric corrected product from the L1T product; L8 PANSH) data was tested in the areas PCG located in Spain, Morocco, Italy and Turkey. The six corresponding bands of S2 and L8, along with the normalized vegetation difference index (NDVI), were generated via an OBIA approach for each PCG study site. The coefficient of determination (r^2) and mean square error (RMSE) were calculated in sixteen pairs of simultaneously cloud-free images acquired from the four study sites to assess the coherence between the two sensors. It was found that the S2 and L8 correlation (^{r2}> 0.840, RMSE <9.917%) was quite good in most bands and NDVI. However, the correlation of the two sensors

fluctuated between study sites, showing occasional solar flare on PCG roofs relative to the sensor's orbit and the position of the sun. Furthermore, higher surface reflectance discrepancies were always observed between the L8 L2 and L8 PANSH data, mainly in the bands visible in areas with high level aerosol values derived from the aerosol quality band included in the L8 L2 product (aerosol SR). In this way, the coherence between L8 PANSH and S2 L2A was improved mainly in the high-level aerosol areas according to the SR aerosol band.

1.2.4 Aims of this work

This thesis will analyze innovative classification procedures with the aim of reducing the negative impacts related to the spectral ambiguity and spatial complexity of the land cover classes of the VHR images in the Bari study sites with a high prevalence of plastic coverings for agriculture. In order to avoid these disadvantages, the methodology will be based on object-oriented classification on Deimos-2 high resolution images (1 m GSD PAN and 4 m GSD RGBNir MS) and on the spectral values obtained from a time series of Sentinel-2 images. The analysis consists of two phases: multi-resolution segmentation and classification of the nearest neighbor of the resulting image objects. With this procedure the generated segments act as image objects whose physical and contextual characteristics can be described using fuzzy logic. Finally, the validity and limits of this methodology for the classification of land cover will be evaluated and the results obtained will be compared with those of the previous studies in relation also to the characteristics of the study site in Bari.

1.3 Study site

1.3.1 Location

The site is located in the Puglia region (southern Italy), near Bari. Satellite imagery were acquired around the point with geographic coordinates (WGS84 reference system) 41.0166 N and 16.9119 E (Fig. 4).

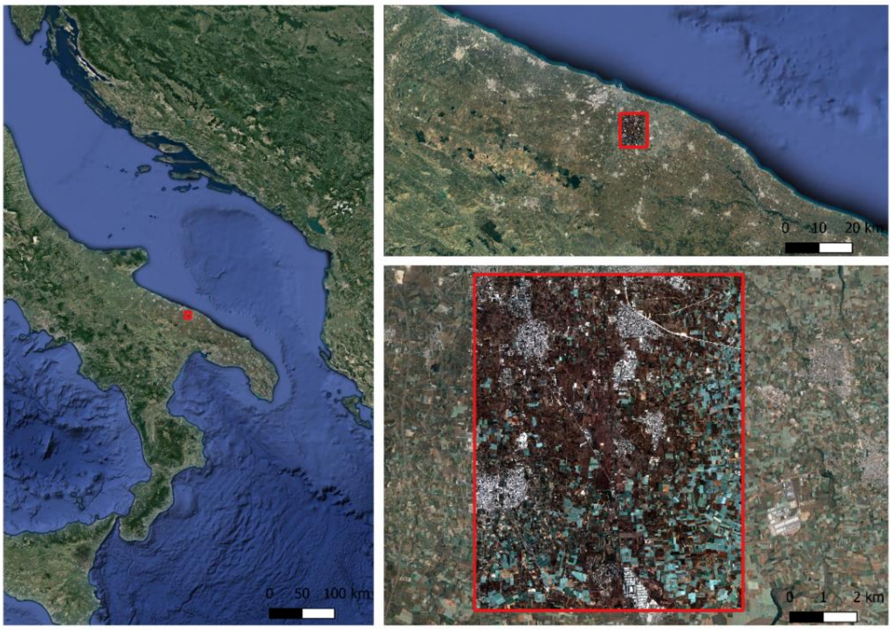

(Fig.4 - Bari study site)

In this area there is a monoculture in the vineyard, where they grow using the traditional vine cultivation system characterized by a support structure covered with plastic sheets in spring and summer. The area has a rectangular shape with an area of approx. 8000 ha (8,000 m x 10,000 m) and the topography is quite flat.

1.3.2 Apulian viticulture

Table viticulture in Italy is predominantly present in Puglia and Sicily. Puglia holds the leading production. Minor productions are also located in Abruzzo. The particular climatic conditions, which are characterized by the singular poverty of its rainfall, and the stony and calcareous soils, in which the rock often emerges, make wheat cultivation unprofitable and allow the farmer only the choice of a few plants to cultivate, which in normal periods and for exceptional and transitory causes give the greatest income. Apulian viticulture greatly affects the economy of the entire region, so much so that it determines and constitutes a real social issue (LE STORIE, I PROTAGONISTI, LE NOVITÀ., s.d.). All the systems to date are protected with plastic roofing materials which differ essentially in polyethylene films. The breeding system that made it possible to better prepare the structures for protection with plastic materials was the tent introduced in Puglia in the early 1900s. The success of the marquee in the cultivation of table grapes, however, lies first and foremost in the ability to express an exceptional production potential and considerable flexibility in facilitating the contribution of agronomic and technological innovation that the production cycle of table grapes continuously requires. The awning allows to reach productions of 40 tons per hectare. Furthermore, the productions of this type of plant have been able, over time, to be always characterized by the regularity and uniformity of the morphological and commercial characteristics. The results achieved were made possible also thanks to the possibility of facilitating the management of the production factors of table grapes: water supplies, fertilization, soil processing, phytosanitary protection, the ability to host protective structures. Plastic film covers are used in viticulture to anticipate the ripening period of early and very early table grape varieties (early semi-forcing) or to delay the ripening period (late semi-forcing) on medium-late varieties or late. In the first case the vineyard is covered, on the top and on the sides, from the end of winter until the harvest, with special plastic films. In the late semi-hardening, on the other hand, the covering period coincides with the veraison phase - before the rains of late summer - and in this case the plastic film is applied only on the top. These two classic management systems have been joined by a third consisting of the upper covering of the structure with plastic film starting from the bud break stage (Luigi Tarricone, 2021).

1.3.3 Technique of using plastic covers

The placement of these artifacts on the vineyard takes place at bud break. Throughout the production cycle they allow to create a confined environment in which better growth conditions are determined. In fact, in the central periods of summer there is less transpiration and a better relaxation of the vegetative structures and bunches. In summary, these breeding conditions lead to an increase in production of 10-15% in unit yields per hectare. In the technique of postponing harvesting, the nets are placed at bud break and the sheets are mounted on them from mid-August until late autumn. The latest innovations try to condense the management of the two production techniques. Today, in fact, the most recent solution in the management of protections provides for the combined use of fabric and net products. The net is placed outside while the sheets are mounted inside. This guarantees the production against fungal attacks that can occur in particularly rainy springs. In this way a better anchoring and protection of the film from the wind and a reduction of temperature peaks are also guaranteed. In fact, it is possible to collect the flaps of the cloth while maintaining the protection of the net. Furthermore, the protective action of the mesh allows you to mount, at the bottom, a film of lesser thickness and, therefore, less expensive.

1.3.4 Effects on the landscape and rural territory

The effects that the protection systems of table grape awnings determine on the territory concern above all the influence on the rural landscape, due to the large surfaces of light and reflective color with chromatic changes and the effect of "liquid mirror" or "agricultural landscape as a chessboard”, and the impact on the agro-ecosystem. In particular, the problem of impact is identified in the need to dispose of large quantities of post-consumer plastics, which can cause negative consequences on the environmental compartments soil, water and air in the event of abandonment on the territory and uncontrolled combustion. The solution consists in a correct management of the phases of disposal, collection, transport and recycling of the plastic material used, which must be considered not a waste but a secondary raw material.

(Fig.5 – Viticulture near Bari)

1.4 Datasets

1.4.1 Deimos-2

DEIMOS-2 is a high-resolution satellite that acquires multispectral images in 4 bands with a resolution of 4 m (resampled to 1 m in the multispectral), and 1 m (resampled to 75 cm in the panchromatic). As a result, the standard pan-sharpened (ortho) product has a resolution of 75cm after resampling. Launched on 19 June 2014, for a mission lasting about seven years, the satellite operates from a helium-synchronous orbit at an altitude of 620 km with local time 10.30 in ascending node (Fig. 6). DEIMOS-2 has a high-resolution on-board sensor with 5 spectral channels (1 panchromatic, 4 multispectral) and is capable of acquiring both monoscopic and stereoscopic images (Table 1). The number of application fields in which DEIMOS-2 images can be used is considerable. From precision agriculture, to emergency management, to environmental and vegetative monitoring, to the updating of thematic maps. DEIMOS-2 includes a panchromatic sensor and a multispectral sensor that acquire in simultaneous mode.

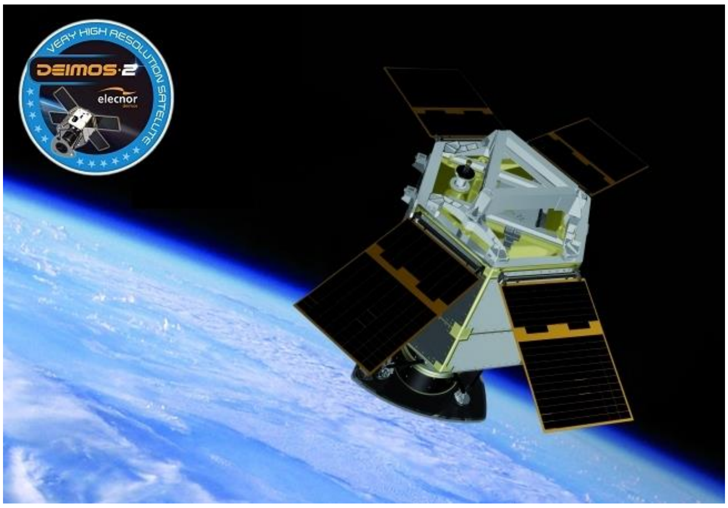

(Fig. 6 – Deimos-2 satellite)

The multispectral band includes the 4 visible channels and the near IR band. The images are distributed in two different processing levels. The Level 1B (L1B) product provides calibration and radiometric correction, but does not include resampling on a map grid. This basic product includes RPCs (sensor camera model) and metadata with gain and bias values for each band. The level 1C product (L1C) turns out to be a more elaborate product that has been calibrated and radiometrically corrected.

Multispectral Bands	Technical features
Blue: 466 nm – 525 nm Green: 532 nm – 599 nm Red: 640 nm – 697 nm NIR: 770 nm – 892 nm	Resolution: 1m resampled to 75cm Width of the strip: 12 km to the nadir Acquisition capacity: 200,000 km^2 per day Average review time: 2 days

(Table 1 – Deimos-2 features)

Deimos-2 was designed to provide a cost-effective and highly responsive service to cope with the increasing need of fast access to sub-metric imagery. As evidence of this, it provides near-real time image tasking, downloading, processing and delivery to the end user. It has a collection capacity of more than 150,000 km2/day with a two-day average revisit time worldwide. The whole Deimos-2 ground segment has been completely developed in-house by Elecnor Deimos based on its own gs4EO product suite, born out of the know-how acquired during more than a decade of work for the European Space

Agency. A single Orto pansharpened image taken on July 29, 2020 on the study area was acquired.

1.4.2 Sentinel-2

The Copernicus Sentinel-2 mission includes a constellation of two polar orbiting satellites placed in the same orbit synchronous with the sun, in phase 180° with respect to each other (Sentinel-2A and Sentinel-2B). In recent years, the two twin European satellites in polar orbit, Sentinel-2A and Sentinel-2B have been used extensively as a single source of data to map plastic-covered agricultural areas. It aims at monitoring the variability in the earth's surface conditions and its wide swath width (290 km) and high revisit time (10 days at the equator with one satellite and 5 days with 2 satellites in cloudless conditions which result in 2-3 days at mid-latitudes) will support the monitoring of changes in the Earth's surface. The images used in this work were acquired by Sentinel-2A (S2A) MultiSpectral Instrument (MSI) which was launched in June 2015. The MSI sensor collects up to 13 bands with three different geometric resolutions ranging from 60m to 10m GSD. The SENTINEL-2 products available to users (generated from the ground segment or the SENTINEL-2 Toolbox) are listed in Table 2.

Name	High-Level Description	Production & Distribution	Data Volume
Level-1C	Top-Of-Atmosphere reflectances in cartographic geometry	Systematic generation and online distribution	~600 MB (each 100km x 100km^2)
Level-2A	Bottom-Of-Atmosphere reflectances in cartographic geometry	Systematic and on-User side (using Sentinel-2 Toolbox)	~800 MB (each 100km x 100km^2)

(Table 2 - Sentinel-2 Level 1C and Level 2A)

Fifteen S2A MSI level 1C (L1C) images, for each study area, well distributed over the year 2020, were downloaded free of charge from the website of the European Space Agency (ESA) Copernicus Scientific Data Hub tool. They were used as input data for the binary pre-classification of greenhouses and non-greenhouses and the subsequent classification of the type of greenhouse cultivation.

	Bari	
Date	***Satellite***	***Orbit***
25/1/2020	2B	R036
9/2/2020	2A	R036
13/3/2020	2A	R079
17/4/2020	2B	R079
9/5/2020	2A	R036
28/6/2020	2A	R036
3/7/2020	2B	R036
23/7/2020	2B	R036
2/8/2020	2B	R036
12/8/2020	2B	R036
27/8/2020	2A	R036
7/9/2020	2A	R036
6/10/2020	2A	R036
31/10/2020	2B	R036
15/11/2020	2A	R036

(Table 3 – Sentinel 2 Images)

After downloading, for each image, all the packages containing the bands for the various resolutions, the bands (Table 4) have been selected:

Nº orden stack	Band	Resolution	Central Wavelenght (µm)
1	Band 2 –Blue (B)	Resolution 10 m	0.443
2	Band 3-Green (G)	Resolution 10 m	0.560
3	Band 4 –Red (R)	Resolution 10 m	0.665
4	Band 5 -Red edge 1 (RE1)	Resolution 20 m	0.705
5	Band 6 -Red edge 2 (RE2)	Resolution 20 m	0.740
6	Band 7 -Red edge 3 (RE3)	Resolution 20 m	0.783
7	Band 8 -Nir 1 (NIR8)	Resolution 10 m	0.842
8	Band 8A -Nir 2 (NIR8a)	Resolution 20 m	0.865
9	Band 11 -Swir 1 (SWIR1)	Resolution 20 m	1.610
10	Band 12 -Swir2 (SWIR2)	Resolution 20 m	2.190

(Table 4 - Sentinel-2 L2A image bands)

These bands have been chosen because they are indispensable for the calculation of the various indices in the following paragraphs. All bands selected, for each Sentinel image, have been uploaded to Qgis. With a plug in called SCP (necessarily to be downloaded) it was possible to obtain a single image having all 10 bands. Developed by Luca Congedo, the Semi-Automatic Classification Plugin (SCP) is a free open source plug-in for QGIS that allows semi-automatic classification (also known as supervised classification) of remotely sensed images. It provides several tools for free image download, pre-processing, post-processing and raster computation. The overall goal of SCP (Fig.7) is to provide a set of interconnected tools for raster processing in order to create an automated workflow and facilitate land cover classification, which could also be done by people whose primary field is not the remote sensing

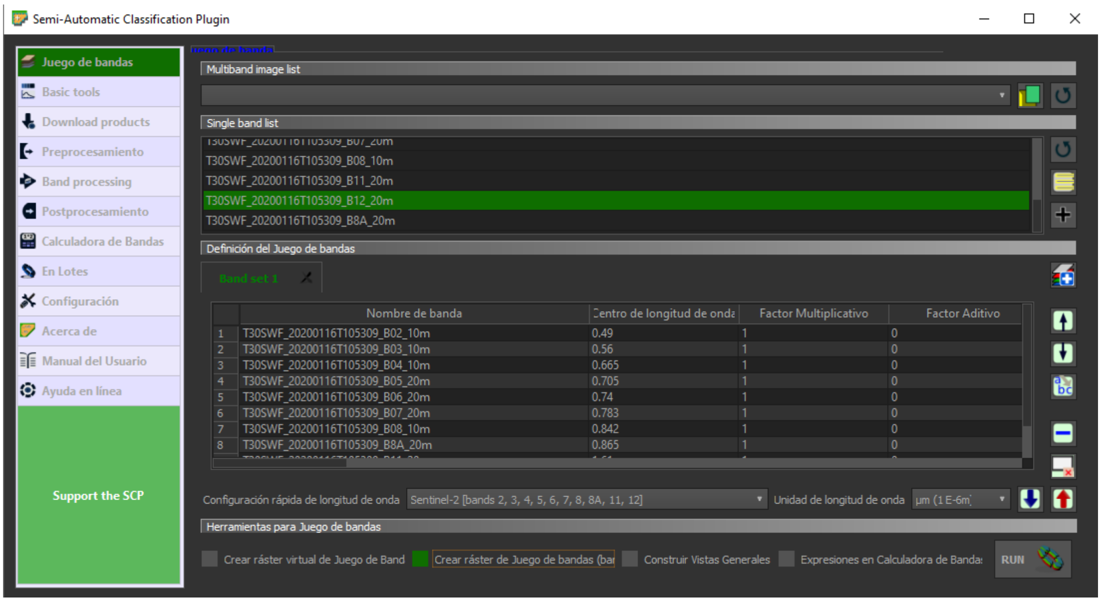

(Fig.7 – SCP plug in)

The images used in this work (Table 3) were collected according to their corresponding study area. Each cropped S2A MSI L2A image was co-registered with the reference image (Deimos-2 pan-sharpened orthoimage) using 44 ground control (Fig. 9, Table 5) points evenly distributed over the study area and a first-order polynomial transformation. The RMSE values for geometrically corrected images were evaluated on 15 ICPs (Fig. 10), ranging from 4.77 m to 5.03 m.

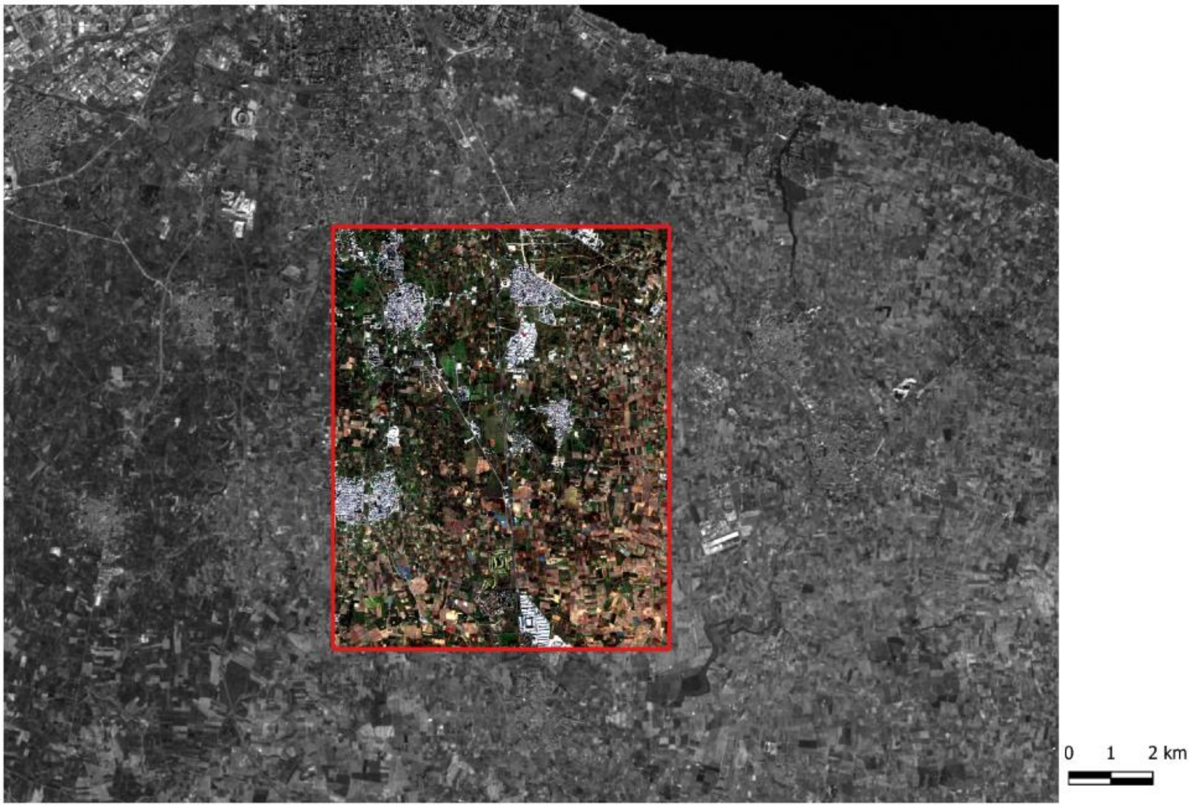

(Fig.8 - Sentinel image collected and with joined bands, January 2020)

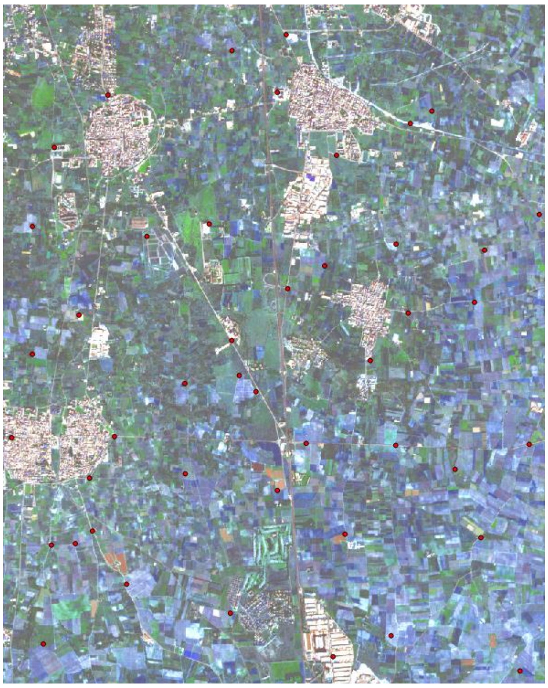

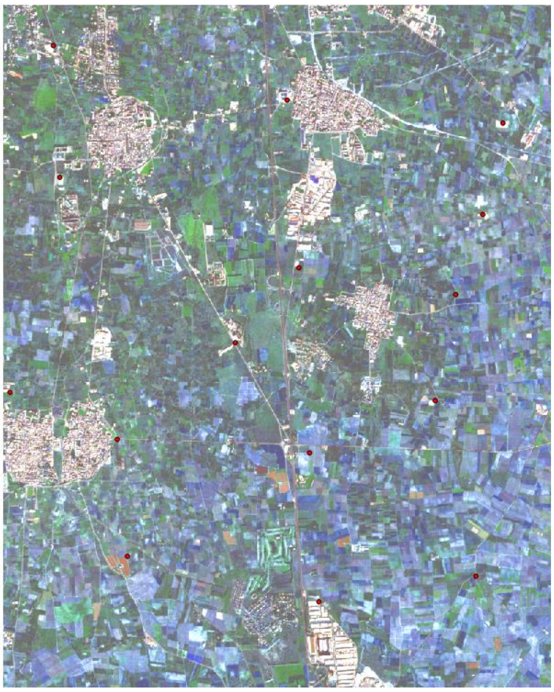

(Fig. 9 - 44 GCP; Fig. 10 – 15 ICP)

GCP	Origen X	Origen Y	Dest. X	Dest. Y	dX	dY	RMSE
0	657430	4546630	657426	4546632	3,99	-2,14	3,203
1	658990	4547050	658985,9	4547054	3,91	-4,04	3,975
2	660520	4546480	660527	4546476	-6,74	3,73	5,447
3	660880	4546770	660874,9	4546774	4,87	-4,16	4,529
4	662090	4547080	662088,6	4547084	1,09	-3,76	2,767
5	662985	4546925	662982,7	4546926	1,93	-1,55	1,750
6	664070	4545520	664066,8	4545523	3,41	-3,30	3,353
7	663020	4546270	663010,9	4546263	8,70	7,85	8,287
8	661509	4545854	661505,4	4545860	4,05	-6,03	5,137
9	658821	4545800	658816,7	4545800	4,76	-0,22	3,366
10	657581	4544600	657578	4544598	2,55	2,38	2,463
11	660670	4543850	660663,1	4543858	7,11	-8,17	7,659
12	663361	4544529	663363,1	4544524	-2,22	5,18	3,986
13	663110	4543400	663104,8	4543407	5,06	-6,90	6,049
14	660120	4545650	660113,9	4545661	6,00	-10,33	8,447
15	658140	4542540	658139,1	4542549	1,21	-8,70	6,211
16	657060	4540050	657055	4540054	4,81	-3,78	4,323
17	657330	4539004	657327,2	4539010	2,40	-5,99	4,560
18	658350	4539190	658360,6	4539192	-10,87	-2,66	7,910
19	659440	4540850	659436,9	4540857	3,03	-6,83	5,284

20	659390	4541661	659389,2	4541661	0,42	-0,77	0,617
21	662661	4542612	662662,5	4542612	-1,43	0,19	1,018
22	661850	4537851	661857,9	4537848	-7,95	2,40	5,868
23	662400	4540830	662395,1	4540834	4,76	-3,86	4,333
24	659750	4543990	659745,9	4544000	4,03	-9,63	7,380
25	660830	4542190	660831,5	4542197	-1,31	-6,82	4,913
26	660709	4539411	660702,7	4539413	6,73	-2,59	5,096
27	664351	4537509	664355	4537516	-4,16	-6,71	5,585
28	663490	4539710	663483,9	4539713	6,22	-3,09	4,911
29	662017	4539332	662014,1	4539336	3,00	-4,34	3,729
30	659599	4537601	659597,1	4537603	1,92	-2,12	2,021
31	664480	4543058	664479	4543063	1,40	-4,57	3,383
32	663058	4541784	663055,5	4541788	2,96	-4,17	3,613
33	661569	4544670	661564,9	4544666	4,40	3,23	3,860
34	664659	4540869	664649,9	4540866	9,19	2,87	6,804
35	658880	4543501	658873,8	4543495	6,36	5,12	5,771
36	657360	4537780	657355,5	4537786	4,26	-6,02	5,215
37	656870	4541670	656873,5	4541674	-3,65	-3,82	3,735
38	660360	4541700	660361,6	4541706	-1,66	-6,47	4,725
39	660900	4543040	660896,6	4543051	3,49	-11,34	8,388
40	663720	4544080	663714,2	4544075	5,71	4,70	5,229
41	662416	4537960	662414,2	4537965	1,60	-5,31	3,917
42	658360	4540880	658357,3	4540883	2,66	-3,52	3,118
43	661270	4540071	661265,3	4540073	5,00	-2,39	3,917
					RMSE X	**RMSE Y**	**RMSE TOT**
					4,77	**5,0339**	**5,033**

(Table 5 – RMSE GCP)

ICP	origen X	origen Y	dest. X	dest. Y	dX	dX	RMSE
0	657425	4546633	657426,6	4546632	-1,33	1,09	1,215
1	660834	4545833	660835,2	4545836	-1,34	-3,20	2,455
2	663976	4545498	663979,1	4545500	-3,37	-1,91	2,737
3	657519	4544709	657520,9	4544708	-1,43	1,10	1,274
4	661002	4543387	661005,5	4543389	-3,76	-1,23	2,793
5	663683	4544163	663686	4544167	-3,45	-3,44	3,446
6	663582	4538879	663585,8	4538884	-3,67	-4,17	3,929
7	662988	4541444	662992,4	4541448	-4,63	-3,65	4,167
8	663293	4542994	663291,8	4542997	1,20	-2,99	2,282
9	660075	4542292	660079,7	4542294	-4,68	-2,29	3,682
10	661293	4538506	661297,5	4538510	-4,19	-4,13	4,158
11	661154	4540685	661160,4	4540685	-5,97	0,08	4,224
12	656788	4541572	656794,3	4541570	-6,55	1,64	4,776
13	658501	4539175	658506,2	4539176	-5,51	-0,33	3,899
14	658355	4540884	658357,5	4540883	-2,54	1,07	1,950
					RMSE X	**RMSE Y**	**RMSE TOT**
					3,95	**2,52**	**3,315**

(Table 6 – RMSE ICP)

2 Methodology

The methodology applied in this work addresses the following aspects:

- Pre-processing protocol for S2 images (explained in section 1.4.2);
- Segmentation of the Orthophoto Deimos-2 with 1 m GSD and 4 bandas (B1: NIR, B2: RED, B3: GREEN and B4: BLUE) taken in Bari (Italy) (29-7-2020) to delineate the greenhouses;
- Binary pre-classification of the entire study area into two classes (GH and Non-GH) by applying an OBIA approach based on Deimos-2 orthoimage segmentation and data from Sentinel-2 image time series;
- Calculation of the various indices inherent to the study and statistical analysis;
- Final classification of greenhouses using the most robust statistical element;
- classification accuracy analysis;

2.1 OBIA approach

OBIA (Object-based Image Analysis) techniques rely on the aggregation of similar pixels to obtain homogeneous segments (often referred to as objects). Then image classification is performed on objects (rather than pixels) using meaningful characteristics related to spectral information (e.g. average spectral values), shape, texture and context associated with each object, so that it has great potential for efficiently handle more difficult image analysis tasks , especially when working on VHR satellite imagery. The quality of the segmentation significantly influences the final results of OBIA approaches since it is this first step that generates image objects and determines their corresponding attributes. Image segmentation is affected by many factors such as image quality, number of spectral bands, spatial resolution and scene complexity.

2.2 Multi-resolution segmentation

Multi-resolution segmentation (MRS) has been listed as one of the most successful image segmentation algorithms in OBIA-type analysis and is available in eCognition software (Trimble, Sunnyvale, California, United States). The performance of this algorithm depends on the selection of three main parameters:

- The homogeneity criterion or scale parameter (SP) which determines the maximum heterogeneity allowed for the resulting segments;
- The weight of color and shape criteria in the segmentation process (Shape);
- The weight of the compactness and smoothness criteria (Compactness).

In this study, the segmentation (MRS) was carried out by means of a semi-automatic eCognition rule set characterized by a loop process that varies the segmentation parameters as follows: the shape values range from 0.1 to 0.5 (with a step of 0.1); Compactness has been set at 0.5 for all cases as the literature has underlined its minor contribution with respect to the parameters of shape and, above all, of scale; the scale parameter has varied from 80 to 250 (with a step of 1). The combination of the bands for the orthoimage is fixed on equally weighted blue-green and NIR2 bands. It is necessary to consider that the accuracy of the final classification for greenhouses will strongly depend on the automatic segmentation process carried out on the Deimos-2 orthoimage. Hence, it was decided to conduct a manual digitization to obtain the best possible segmentation file on our objects of interest. Up to 400 polygons representing individual plastic greenhouses, were manually digitized on the whole working area into the Deimos-2 orthoimage, all presenting a uniform spatial distribution around the study area, in order to have a representative sample of all the greenhouses of the study area. These reference geometry sets were applied to study the quality assessment of supervised segmentation performed using AssesSeg.

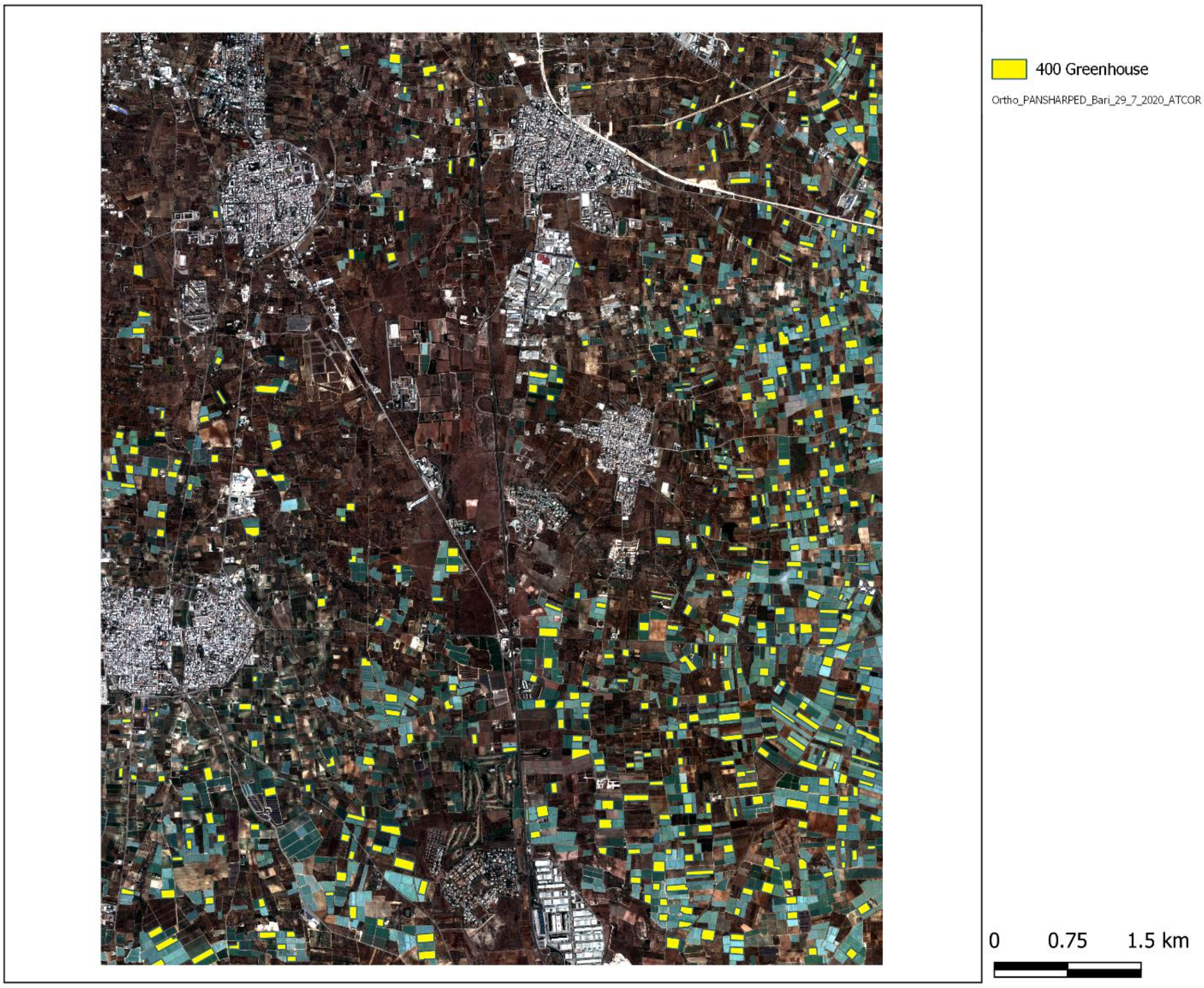

(Fig.11 – 400 Greenhouse objects)

2.2.1 Segmentation Assessment

Although there are several methods to quantitatively assess the quality of the segmentation, the ED2 measure was the one used in this work providing good results on plastic greenhouses. In short, ED2 aims to optimize, on a two-dimensional Euclidean space, both the geometric discrepancy (potential segmentation error (PSE)) and the arithmetic discrepancy between image objects and reference polygons (segmentation number ratio (NSR)).

$$\mathrm{ED2} = \sqrt{(\mathrm{PSE})^2 + (\mathrm{NSR})^2}$$

(Fig.12 – ED2 expression)

The modified version of ED2 was included in a command line tool called AssesSeg and it was tested on different satellite images (Sentinel-2, Landsat 8, and WorldView-2). The software deals only with the ESRI polygon shapefile (it does not depend on the segmentation software), and its source code was written in Python 2.7 given the large availability of open source optimization, data analysis, control, and numerical analysis libraries. AssesSeg outputs were utilized to find the best band combinations for the performed segmentations of the images and showed a clear positive correlation between segmentation accuracy and the quantity of available reference data. This demonstrates the importance of a high number of reference data in supervised segmentation accuracy assessment problems. Lastly, AssesSeg is a very powerful tool if coupled with automatic or semi-automatic algorithms capable of producing many segmentation files following a certain criterion. In this work, this was accomplished by means of a semi-automatic eCognition rule set characterized by a looping process among prefixed multi-resolution segmentation (MRS) algorithm parameters. It is important to note that a modified ED2 value of zero would indicate an optimal combination of both geometric and arithmetic match. An optimum geometric match would be related to the absence of over-segments or under-segments. The best arithmetic match would occur when a reference polygon only matches a calculated object MRS. The ideal segmentation will be pointed out by the minimum value of modified ED2 measure.

2.2.2 Segmentation results

The best segmentation for the orthoimage was based on the minimum value of the modified ED2 computed for the set of reference geometries (400 polygons). The modified ED2 was a very good result for the visual quality of the greenhouse segmentations. In Figure 13 there are the modified ED2 values calculated for each segmentation extracted from the Deimos-2 orthoimage with respect to the set of 400 reference geometries. The fixed parameters were the combination of bands (Blue-Green-NIR2) and Compactness (0.5), while Shape and Scale were kept variable.

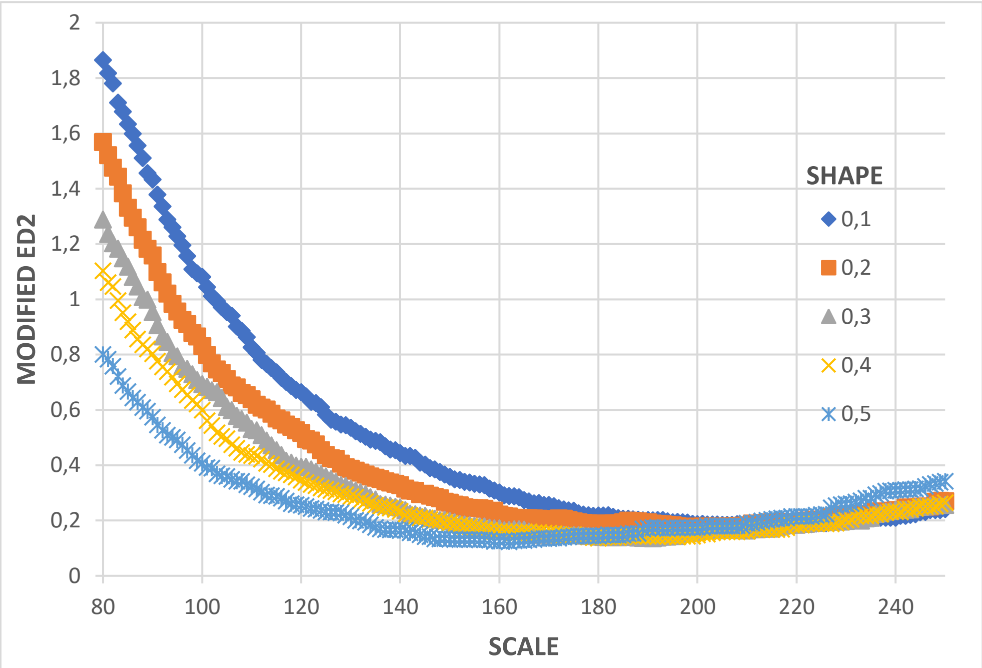

(Fig. 13 - MSR parameters based on the final ED2 values)

In this case, the minimum modified ED2 value was obtained for the shape and scale values described in Table 7.

SCALE	COMPACTNESS	SHAPE	ED2
162	0.5	0.5	0.12232

(Table 7 – best segmentation)

This figure also allows to appreciate the importance of testing a wide range of parameters to find out the ideal segmentation.

2.3 Classification

2.3.1 Binary Pre-Classification

The binary pre-classification assigned a class (GH or Non-GH) to each previously segmented object in the study area. A dataset consisting of 1500 segments for the GH class and 1500 for the Non-GH class (i.e., any other object other than a greenhouse), which were homogeneously distributed in the study area. the choice of using 3000 objects in the pre-classification has already been used by (Manuel A. Aguilar A. N., 2016) and (Abderrahim Nemmaoui, 2018). The best segmentation achieved from the Deimos-2 image with AsseSseg was used and a new edited thematic layer was generated from it. A new column called "class" has been inserted into the attribute table of the SHP file. Non-GH segments were classified with the number 2, while the GH objects with the number 1. Furthermore, a new column has been added in the attribute table that assigns an ID number to each segment so that they can be immediately tracked for any anomalies in future calculations. During the classification process it is extremely important to select segments where the pixels within are of the same class so that nothing is mixed. The Bari study area is characterized by a variable presence of greenhouses throughout the year. This is due to the type of seasonal crop present inside the greenhouses. Therefore the pre-classification was made based on both the Deimos-2 image and the Sentinel-2 time series, in order to achieve a better pre-classification. The low geometric resolution of the Sentinel-2 images (10m) compared to the Deimos-2 image could be a problem for classification. For this reason, a combination of band was selected such as to make clear the spectral difference between the areas covered by GH and areas not covered.

(Fig. 14 – Sentinel-2 image with spectral combination: R->SWIR2; G->SWIR1; B->B)

(Fig. 15 -Classification of Deimos-2: Red-> GH; Blue->Non-GH)

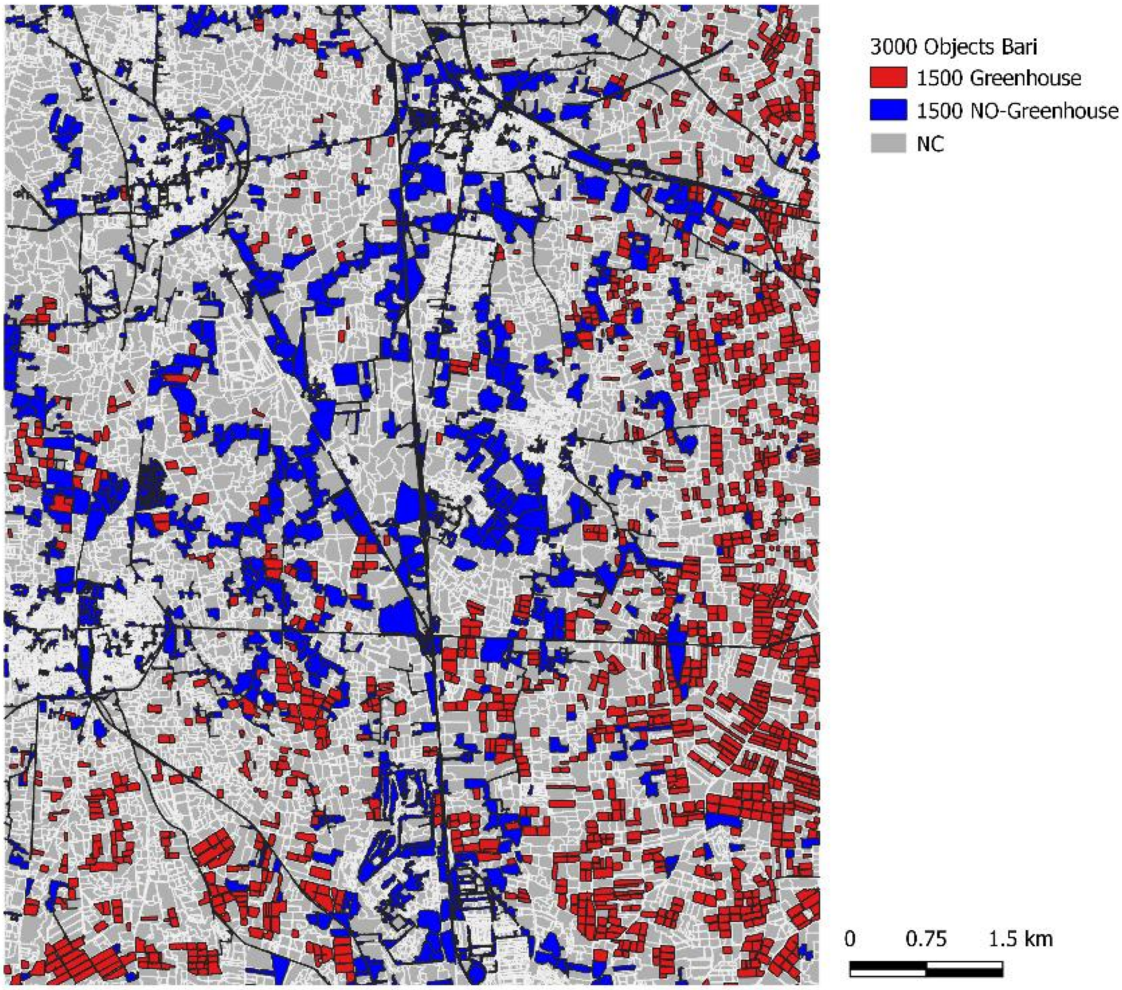

(Fig. 16 – Binary pre-classification)

2.3.2 Features

The object-based features that were used in this work to accomplish the two-step OBIA classification (binary pre-classification in GH and Non-GH classes) were retrieved from the S2 images (10 bands) image time series. The features consist of several spectral and vegetation indices for S2 (14 indices) single images. Note that one specific object (a greenhouse, for instance) will have 14 single values for each object-feature. Table 8 shows the object features tested in this study. The selection of the features was mainly based on the results of previous researches.

Index	abbreviaton S2	Description	Reference
Moment Distance from the Right pivot	**MD_{RP}**	((SWIR2/10000)+((SWIR1/10000)^2+(2.19-1.61)^2)^0.5+((NIR8a/10000)^2+(2.19-0.865)^2)^0.5+((NIR8/10000)^2+(2.19-0.842)^2)^0.5+((RE3/10000)^2+(2.19-0.783)^2)^0.5+((RE2/10000)^2+(2.19-0.74)^2)^0.5+((RE1/10000)^2+(2.19-0.705)^2)^0.5+((R/10000)^2+(2.19-0.665)^2)^0.5+((G/10000)^2+(2.19-0.56)^2)^0.5+((B/10000)^2+(2.19-0.49)^2)^0.5)	Salas and Henebry (2012)
Moment Distance from the Left pivot	**MD_{LP}**	((B/10000)+((G/10000)^2+(0.56-0.49)^2)^0.5+((R/10000)^2+(0.665-0.49)^2)^0.5+((RE1/10000)^2+(0.705-0.49)^2)^0.5+((RE2/10000)^2+(0.74-0.49)^2)^0.5+((RE3/10000)^2+(0.783-0.49)^2)^0.5+((NIR8/10000)^2+(0.842-0.49)^2)^0.5+((NIR8a/10000)^2+(0.865-0.49)^2)^0.5+((SWIR1/10000)^2+(1.61-0.49)^2)^0.5+((SWIR2/10000)^2+(2.19-0.49)^2)^0.5)	Salas and Henebry (2012
Moment Distance Index	**MDI**	**MD_{RP}** – **MD_{LP}**	Salas and Henebry (2012)
Normalized Difference Vegetation Index	**NDVI**	(NIR8 – R)/(NIR8 + R)	Rouse et al. (1973)
Normalized Difference Builtup Index	**NDBI**	(SWIR1 – NIR8)⁄(SWIR1 + NIR8)	Zha et al. (2003)
Plastic Greenhouse Index	**PGI** (reflectancias en 0-10000)	100 × (B × (NIR8 – R))⁄(1 – (B + G + NIR8)/3) PGI = 0 when **NDVI**>0.73 PGI = 0 when **NDBI**>0.005	Yang et al. (2017)
Plastic Greenhouse Index	**PGI1** (reflectancias en 0-1)	100 × ((B/10000) × ((NIR8/10000))–(R/10000))))⁄(1 – ((B/10000)) + (G/10000)) + (NIR8/10000)))/3) PGI = 0 when **NDVI**>0.73 PGI = 0 when **NDBI**>0.005	Yang et al. (2017)
Retrogressive Plastic Greenhouse Index	**RPGI**	(B/10000)/(1–((B/10000)+(G/10000)+(NIR8/10000))/3)	Yang et al. (2017)
Plastic-Mulched Landcover Index	**PMLI**	(SWIR1 – R)⁄(SWIR1 + R)	Lu et al. (2014)
Greenhouse Detection Index	**GDI**	(**MDI**/3) – ((B – (SWIR1 + SWIR2)/2)/(B + (SWIR1 + SWIR2)/2))	González-Yebra et al. (2018)
Index Greenhouse Vegetable	**Vi**	((SWIR1 – NIR8)⁄(SWIR1 + NIR8)) × ((NIR8 – R)⁄(NIR8 + R))	Zhao et al. (2004)

Land Extraction			
Plastic Index	**PI**	NIR8/(NIR8 + R)	Themistocleous et al. (2020)
Floating Debris Index	**FDI**	(NIR8/10000) – ((RE2/10000)+((SWIR1/10000)–(RE2/10000))×((λ_{NIR}– λ_{RED})/ (λ_{SWIR1}– λ_{RED})) ×10) λ_{NIR}=833 nm; λ_{RED}=665 nm; λ_{SWIR1}=1613 nm	Biermann et al. (2020)

(Table 8 – Indices)

(Dedi Yang, 2017) proposes a new plastic greenhouse index (PGI) based on the spectral analysis, sensitivity and separability of plastic greenhouses using medium spatial resolution images. The results demonstrated that the proposed index can be applied to identify transparent greenhouses in the Landsat image with atmospheric correction and has the potential for digital mapping of plastic greenhouse coverage over

$$\mathrm{PGI} = \begin{cases} 0 & \text{When NDVI} > 0.73 \\ 100 \times \frac{R_{blue} \times (R_{nir} - R_{red})}{1 - mean(R_{blue} + R_{green} + R_{nir})} & \\ 0 & \text{When NDBI} > 0.005 \end{cases}$$

where

$$\mathrm{NDVI} = \frac{R_{nir} - R_{red}}{R_{nir} + R_{red}}$$

$$\mathrm{NDBI} = \frac{R_{sw1} - R_{nir}}{R_{sw1} + R_{nir}}$$

(Fig. 17 – PGI equation)

a large area. The PG index is expected to be effective for both the PG detection and the PG fraction estimation. Therefore, the design of the PG index should consider the spectral characteristics that best differentiate PG from the background as well as maximize the range of detectable PG fraction. the PG index (PGI) was developed to exaggerate the difference between PGs and other features, as shown in the following equations. In this equation, R-blue, R-green, R-red, R-nir , and R-sw1 are the reflectance of the blue, green, red, NIR, and SW1 band, respectively. The multiplier 100 is used to linearly stretch the PGI to a wider range. To offset the effect of dense vegetation (e.g. forest) and man-made surfaces, pixels with NDVI greater than 0.73 or NDBI greater than 0.005 were treated as non-PG pixels. Anyway, it is problematic to apply an absolute criterion (i.e., PGs or no PGs) to estimate PG area. To overcome this issue, the result is presented in terms of the PGI and the PG fraction. Yang's study developed a statistical model to estimate the PG fraction. The result of (R-nir – R-red) in the PGI may increase the variance of PGI, as the types of crops under PGs and their growth status vary to a certain extent. To enhance the sensitivity of the new index, a retrogressive PGI (RPGI) (Fig. 18), defined by removing the (R-nir – R-red) component and the multiplier in the PGI formula, was proposed to develop a more cohesive and robust measure.

$$\mathrm{RPGI} = \frac{R_{blue}}{1 - mean(R_{blue} + R_{green} + R_{nir})}$$

(fig.18 -RPGI equation)

Another new index used in this work is the GDI, specially designed for PCG mapping. It has been studied and tested in the work of (Oscar Gonzalez-Yebra, 2018). The GDI index integrates the spectral information provided by the MDI index (see Table 8), already successfully tested in (Manuel A. Aguilar A. N., 2016) for PCG mapping, and the relative ground reflectance of PCG in the B band (high) and Swir1 and Swir2 bands (low) (Manuel A. Aguilar A. N., 2016). Note that a low MDI index is related to PCG objects and vice versa. In this sense, the formulation that supports the GDI index can be found in equation on the Figure 19, with the aim of improving the discrimination of greenhouses in the classification process through correcting the MDI index, previously downscaled by dividing it by three to decrease its weight, subtracting a normalized index based on B, Swir1 and Swir2 bands.

$$GDI = \left(\frac{MDI}{3}\right) - \left(\frac{B - \left(\frac{Swir1+Swir2}{2}\right)}{B + \left(\frac{Swir1+Swir2}{2}\right)}\right)$$

(Fig. 19 – GDI equation)

PI, on the other hand, was introduced for the first time by (Kyriacos Themistocleous, 2020). The newly developed Plastic Index (PI) was able to identify plastic objects floating on the water surface and was the most effective index in identifying the plastic litter target in the sea with Sentinel-2 images. In a very similar way, the FDI was introduced in the (Lauren Biermann, 2020) publication to monitor the plastic debris present in the oceans. At 10 m × 10 m, the highest spatial resolution of the Sentinel-2 Multi-Spectral Instrument, individual items of debris are likely to be below detectable limits until aggregated into patches. To improve the detection of spots floating on the ocean surface in Sentinel-2 images, the Floating Debris Index (FDI) was developed using four of the 10 MSI bands (Table 9).

Nº orden stack	**Banda**	**Resolution**	**Central Wavelenght (µm)**
1	Banda 2 –Blue (B)	Resolution 10 m	0.443
2	Banda 3-Green (G)	Resolution 10 m	0.560
3	**Banda 4 –Red (R)**	**Resolution 10 m**	**0.665**
4	Banda 5 -Red edge 1 (RE1)	Resolution 20 m	0.705
5	**Banda 6 -Red edge 2 (RE2)**	**Resolution 20 m**	**0.740**
6	Banda 7 -Red edge 3 (RE3)	Resolution 20 m	0.783
7	**Banda 8 -Nir 1 (NIR8)**	**Resolution 10 m**	**0.842**
8	Banda 8A -Nir 2 (NIR8a)	Resolution 20 m	0.865

9	**Banda 11 -Swir 1 (SWIR1)**	**Resolution 20 m**	**1.610**
10	Banda 12 -Swir2 (SWIR2)	Resolution 20 m	2.190

(Table 9 – Selected bands for FDI)

This debris detection index then takes advantage of the difference between NIR and the base reflectance of NIR. This baseline is derived from linear interpolation between the RE2 and SWIR1 bands flanking NIR:

$$
\begin{aligned}
FDI &= R_{rs,NIR} - R'_{rs,NIR} \\
R'_{rs,NIR} &= R_{rs,RE2} + (R_{rs,SWIR1} - R_{rs,RE2}) \times \frac{(\lambda_{NIR} - \lambda_{RED})}{(\lambda_{SWIR1} - \lambda_{RED})} \times 10
\end{aligned}
$$

(Fig. 20 – FDI equation)

The FDI was applied for subpixel detection of plastic targets deployed off Mytilene in Greece, as well as on dense floating patches of Sargassum seaweed off Barbados, rafted tree logs in waters of British Columbia, sea foam (spume) off the east coast of Scotland, and floating volcanic rock off Tonga. The MDI exploits the available bands of the remote sensing image by analyzing the shape of the reflectance spectrum, and at each composite, calculating the moment distances among the bands through simple geometric operations. The robustness of the method in defining the shape of the spectral curve derives from the refereed distances from two points locations designated as shorter pivot and longer pivot wavelength region, assuming that the reflectance curve is displayed in Cartesian coordinates with the abscissa displaying the wavelength (λ) and the ordinate displaying the reflectance (ρ). The subscript LP denotes the left pivot (located in a shorter wavelength) and subscript RP denotes the right pivot (located in a longer wavelength). λ LP and λ RP are the wavelength locations observed at the left and right pivots, respectively, where left (right) indicates a shorter (longer) wavelength. NDVI was also computed for each polygon, date and study site, using the mean values attained from Red and NIR bands.

2.3.3 Feature extraction

The extraction of the individual object-based features was done within the eCognition software. The idea of introducing the features from Deimos-2 MS orthoimage in the classification process was discarded in order to obtain classification results that were totally independent of the VHR data that was used to carry out the segmentation stage. In other words, the aim was to build a decision tree model only based on S2 features. First, the Sentinel-2 time series images were inserted. All band names have been changed by putting the time series image number and the letter representing the band type.

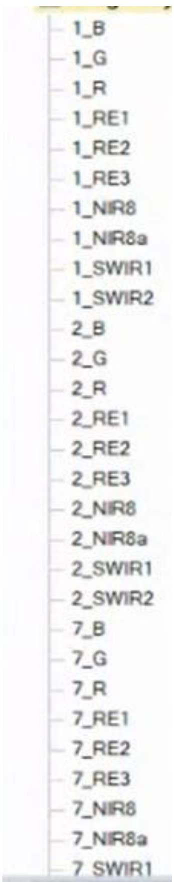

(Fig. 21 - edited band names)

After having edited all the names of the bands, the thematic layer was inserted containing the pre-classification of the 3000 objects made previously. Before starting the data upload, the resolution was set to 0.99984 and the original GSD was halved four times by 15m on the design sheet created to increase geometric resolution. The chessboard segmentation algorithm included in eCognition has been applied on the thematic layer composed of the vector file containing the pre-classification. A chessboard segmentation is the simplest segmentation available as it just splits the image into square objects with a size predefined by the user. The segmentation does not consider the underlying data and therefore when large objects are created, the features within the data you are trying to classify will not be delineated. This segmentation tends to be used in more advanced processes where segmentation is undertaken in a number of steps combined with a classification. Using this approach, the software projects only the vector file into the images in order to obtain an outline adapted to the pixels that compose them.

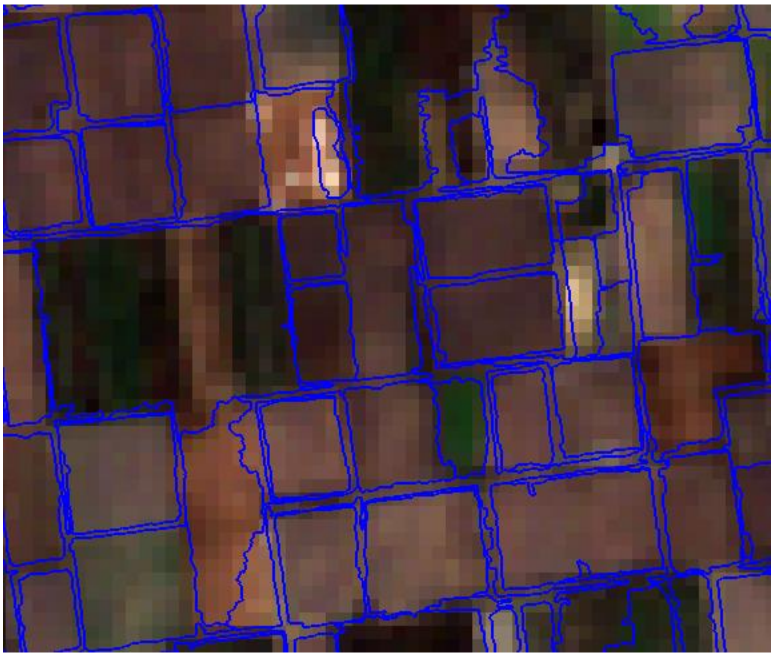

(Fig. 22 – Input Thematic Layer)

At this point it is necessary to introduce the feature formulas into the software, in order to extract an excel file which will subsequently be statistically analyzed. The first step for the creation of the features is to calculate the average value of each band for each image. Therefore 15 mean values were calculated for each band. These average values have been used to create new "arithmetic features" which will be our indices.

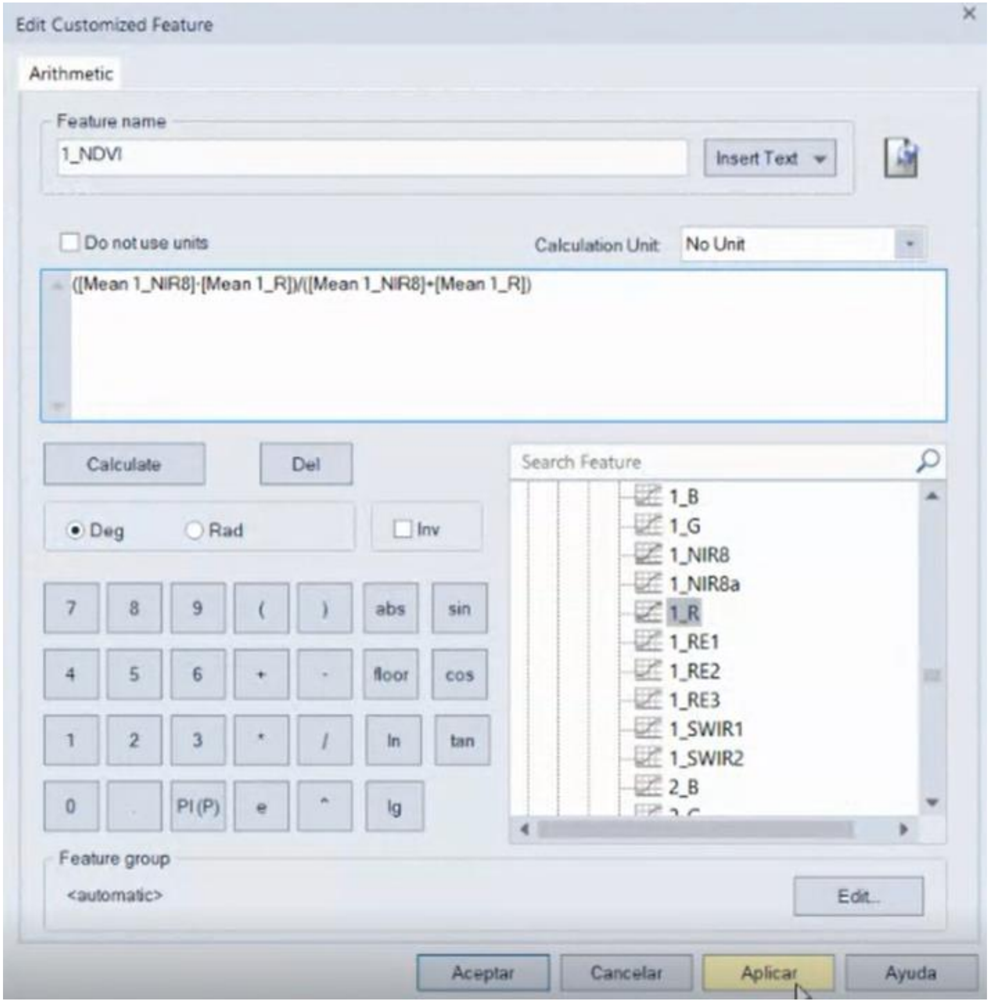

(Fig. 23 - NDVI index calculation)

However, here too, the indices were calculated for each image in the Sentinel-2 time series, so there are 15 values for each index. After inserting all the indices of Table 8 into the project, it is possible to note the values of all the indices in each polygon. Another important thing to be included in the export file is the "class" as it will be a fundamental parameter for the formation of the Decision Tree. The assignment of the class for each segment (classification), before export, was obtained through two steps:

- insert 2 classes (GH -> RED, Non-GH ->BLUE) in the "class hierarchy" part;
- add "assign class" in the software process tree and add the following conditions. For the segments to be GH, the thematic layer values must be "class = 1". Vice versa, for the segments to be Non-GH, the values of the thematic layer must be "class = 2";

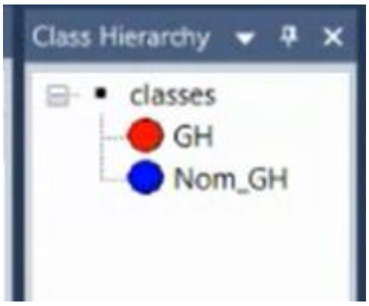

(Fig. 24 - class assignment in ecognition)

At this point the export has been carried out by inserting the values of all the indexes, of the class of each segment, and also of the areas of each segment in such a way as to eliminate segments with areas that are too small which can lead to errors in the classification.

2.3.4 Calculation of statistical features

The output obtained from eCognition data processing is an Excel sheet containing the values of the 14 indices for all 15 S2 images for each polygon.

All polygons not belonging to the GH or Non-GH classification were deleted and in addition, five characteristics were also calculated from the time series of S2 images. These characteristics were MAX (maximum), MIN (minimum), DIF (difference between MAX and MIN), AVERAGE (mean value), SD (standard deviation).

MAX_Vi	MIN_Vi	MEAN_Vi	SD_Vi	DIF_Vi
0,030459	-0,202128	-0,080416	0,082902	0,232588
0,019840	-0,143658	-0,055092	0,045191	0,163498
0,027774	-0,192034	-0,091837	0,067890	0,219807
0,030565	-0,174032	-0,050152	0,060678	0,204596
0,025689	-0,139053	-0,058334	0,058687	0,164743
0,023551	-0,158216	-0,079293	0,068577	0,181767
0,026880	-0,234892	-0,108898	0,096896	0,261772
0,021449	-0,234390	-0,097680	0,082758	0,255840
0,027033	-0,167320	-0,083014	0,075398	0,194352
0,028915	-0,254380	-0,089109	0,083231	0,283295
0,030169	-0,149631	-0,078141	0,065545	0,179800
…	…	…	…	…

(Table 10 - example calculation of statistical values for the "Vi" index)

2.3.5 Decision tree modeling

A decision tree (DT) classifier based on the algorithm proposed by (Breiman, Friedman, Olshen, & Stone) has been used in this work. This classifier presents a very clear structure composed of several splits with single threshold values. In this sense, the DT classifier could be implemented directly in eCognition by means of rule sets to determine simple and robust feature thresholds. DT is a non-parametric rule-based method in which each node makes a binary decision that separates either one class or some of the classes from the remaining class (or classes). Classification through the DT algorithm has already been applied in greenhouse mapping via remote sensing with very good and robust results (Manuel A. Aguilar A. V., 2015) and (Manuel A. Aguilar A. N., 2016). The major reason for its choice lies in that the results from this classifier are simple to understand. The DT classifier is described as a “white box”, because both its structure (formed by several splits) and its final result (terminal leaves) is easy to interpret. Classification through the DT algorithm is increasingly applied in remote sensing data. In fact, it has been the selected classifier in recent OBIA investigations focused on outdoor crop identification. Other advantages of DT classifiers are:

- They fit well in the OBIA procedure;
- DTs are computationally fast and make no assumptions regarding the distribution of the data;
- the DT methods provide quantitative measurements of each variable’s relative contribution to the classification results, so allowing users to rank the importance of input variables;

2.3.6 Statistic analysis

STATISTICA v10 software was used for classification and analysis of the regression decision tree (StatSoft Inc., Tulsa, OK, USA). The software includes an array of data analysis, data management, data visualization, and data mining procedures; as well as a variety of predictive modeling, clustering, classification, and exploratory techniques. in this case study, it was essential to obtain a decision tree through categorical classification. The first step was to add the CSV file (containing the 3000 objects) into the software and select "regression tree model" on "data mining" so that the algorithm can be started. The DT algorithm tries to divide the data into segments that are as homogeneous as possible with respect to the dependent or response variable. In this case, the categorical dependent variable was the class (GH or Non-GH), while the continuous variables were all statistical indices. The final result with this procedure is not affected by data with very high or very low values coming from a single image of the time series. The DT node-splitting rule was the Gini index, which is a measure of impurity for a given node (Zambon, Lawrence, Bunn, & Powell, 2006). Its application attempts to maximize the homogeneity of the child nodes with respect to the values of the dependent variable. Cross-validation provided an objective measure of quality for the computed DT model (2015). The experimental design was implemented within the STATISTICA environment through a stratified 10-fold cross-validation procedure, leading to one confusion matrix for each fold. In 10-fold cross-validation, the data are randomly partitioned into 10 equally-sized samples. Of the 10 samples, a single sample is used to validate the model, and the remaining 9 samples are used to train the model. The cross-validation process is then repeated 10 times, with each of the 10 samples used exactly once as the validation data. The computed DT model was finally applied to the validation dataset to obtain the corresponding confusion matrices. The DT classifier also provides an assessment of the relative importance of the different features or variables during the classification process. This aspect is useful for multi-source studies, where data dimensionality is very high and it is important to know how each predictive variable influences the classification model in order to select the best ones. To assess the importance of each feature, the DT switches one of the input random variables while keeping constant the remaining ones.

2.4 Results

2.4.1 DT classification

Figure 25 shows the DT models computed from S2A image time series based on the 3000 reference objects manually classified as GH or Non-GH. The standard deviation of the Plastic Greenhouse Index (SD_PGI) turned out to be the most significant statistical seasonal feature (first split in the DT model). The PGI proposed by (Dedi Yang, 2017) is a very correlated index to the vegetation under the plastic cover, being higher when the crops inside the greenhouse are thriving. The same result was obtained from the study done by (Abderrahim Nemmaoui, 2018). In that case the classification was made through a comparison of both S2 and L8 time series.

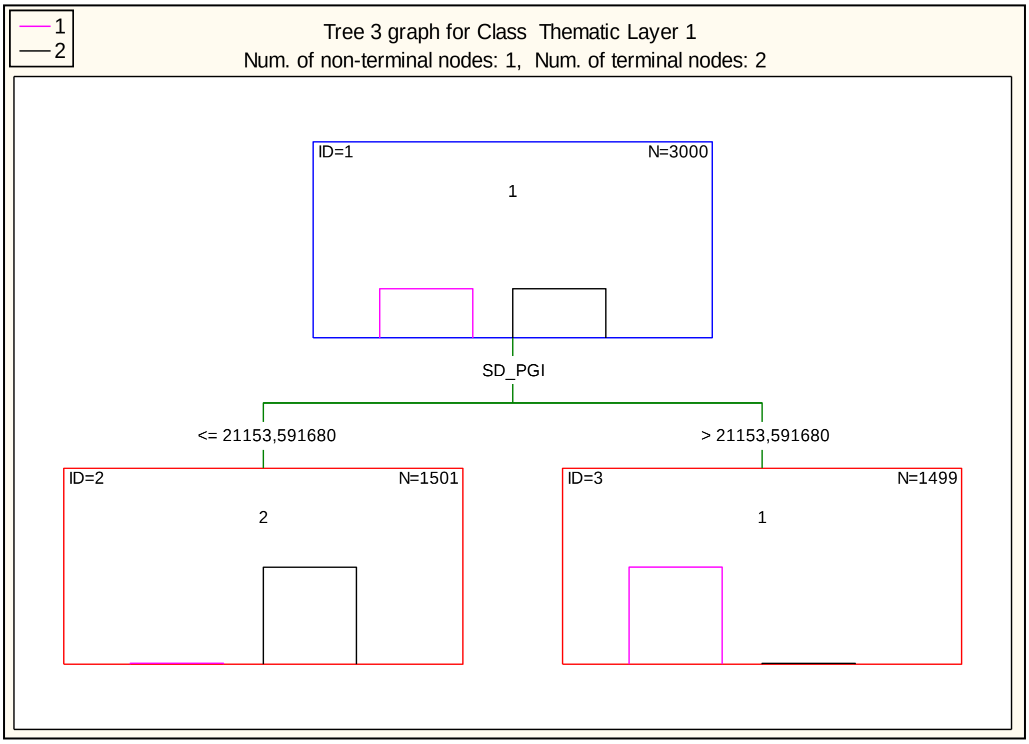

(Fig. 25 – DT model)

The same procedure for calculating the decision tree was done for each image by placing the features as continuous variables. From this setup, a decision tree was extracted for each image in the time series. The highest PGI values were obtained during the period from May to the beginning of November, just when the cultivation of the vine is widespread inside the greenhouses. on the other hand, in the winter months, when there is no large presence of greenhouses in the Bari area, the classification is not guided by the PGI index. The good performance of SD (PGI) feature was actually based on this high range of variability over time to discriminate between GH and Non-GH classes.

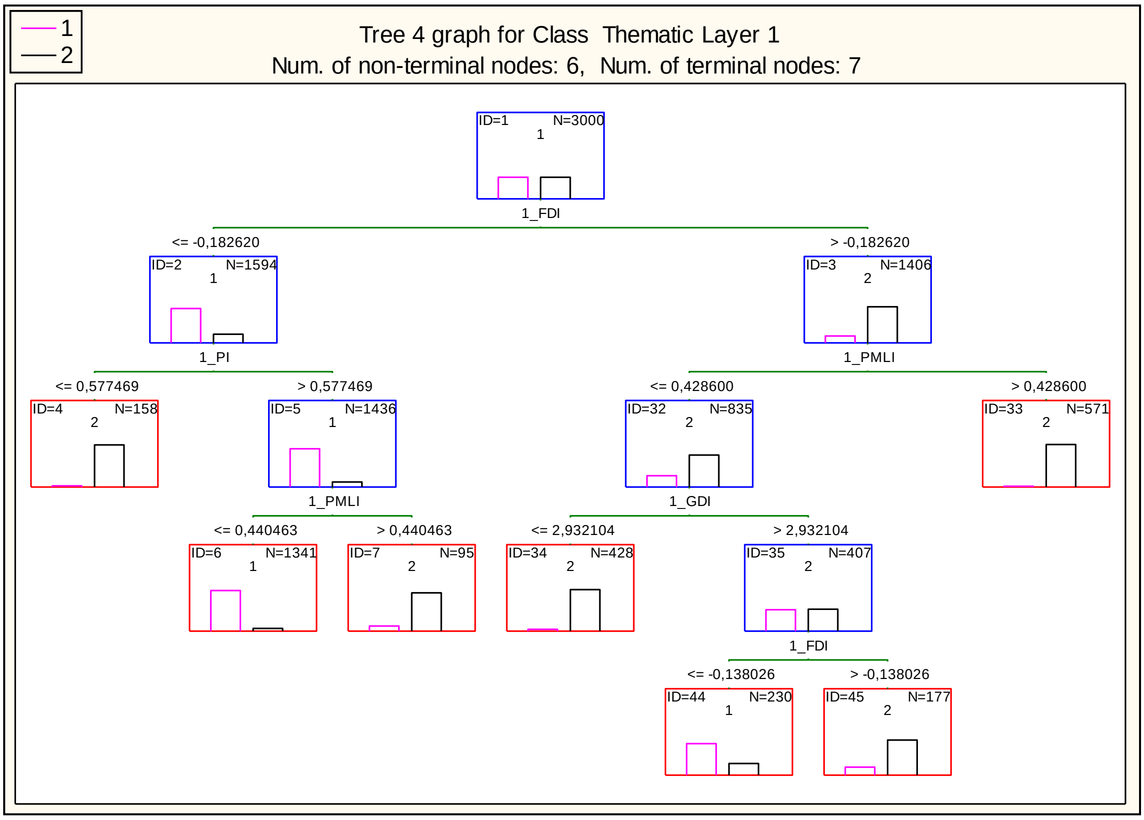

(Fig. 26 - 25/1/2020 Decision Tree)

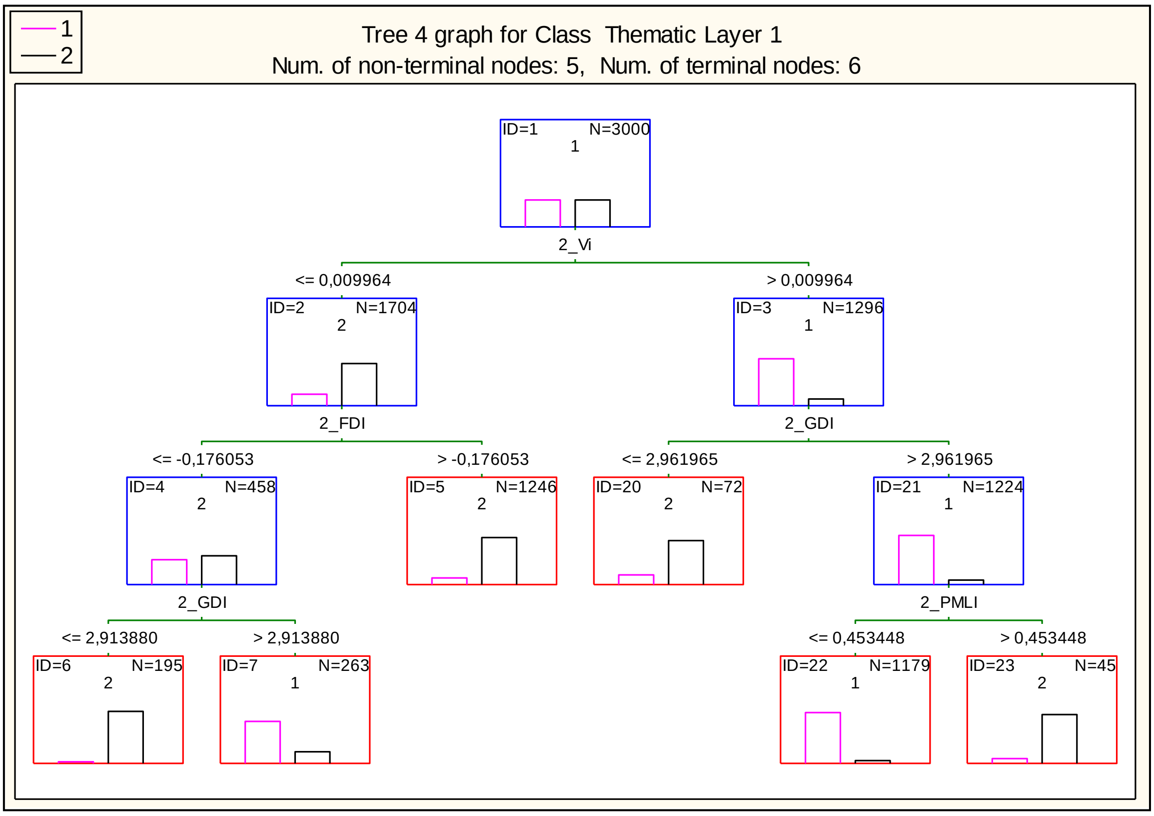

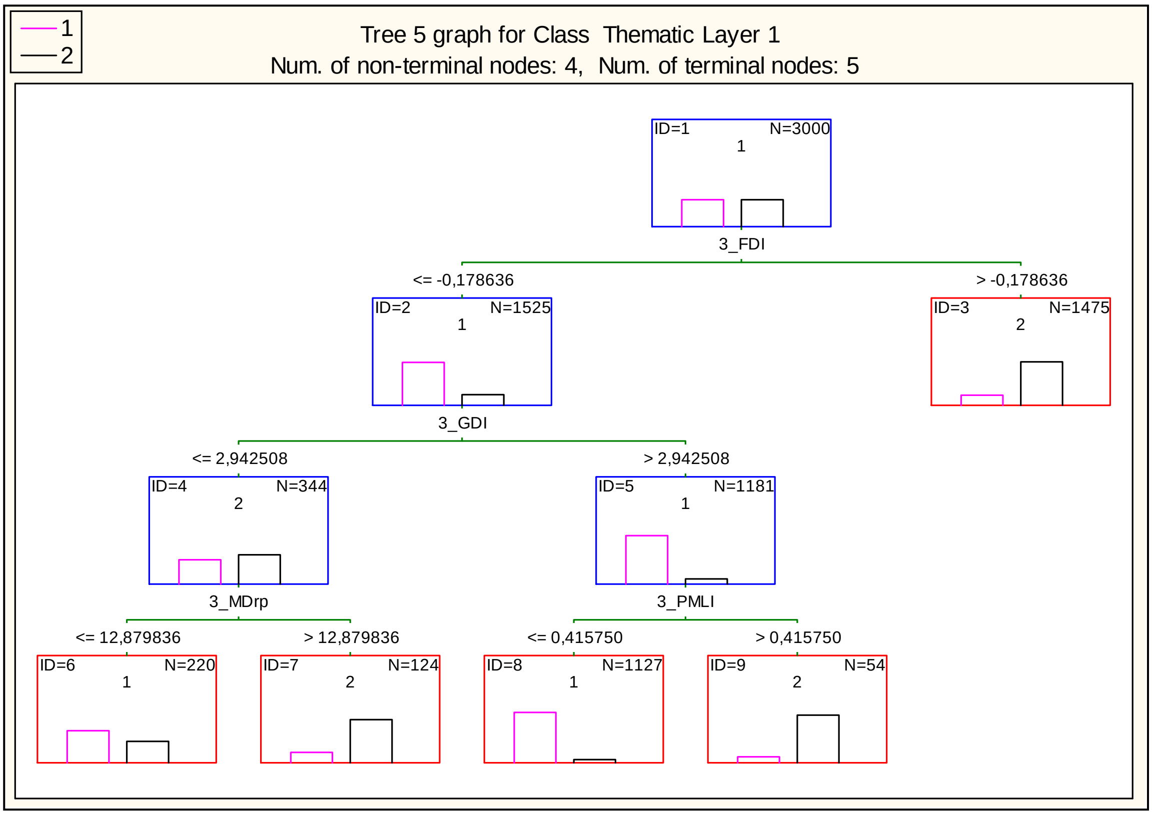

(Fig. 27,28 - 9/2/2020 and 13/3/2020 DT)

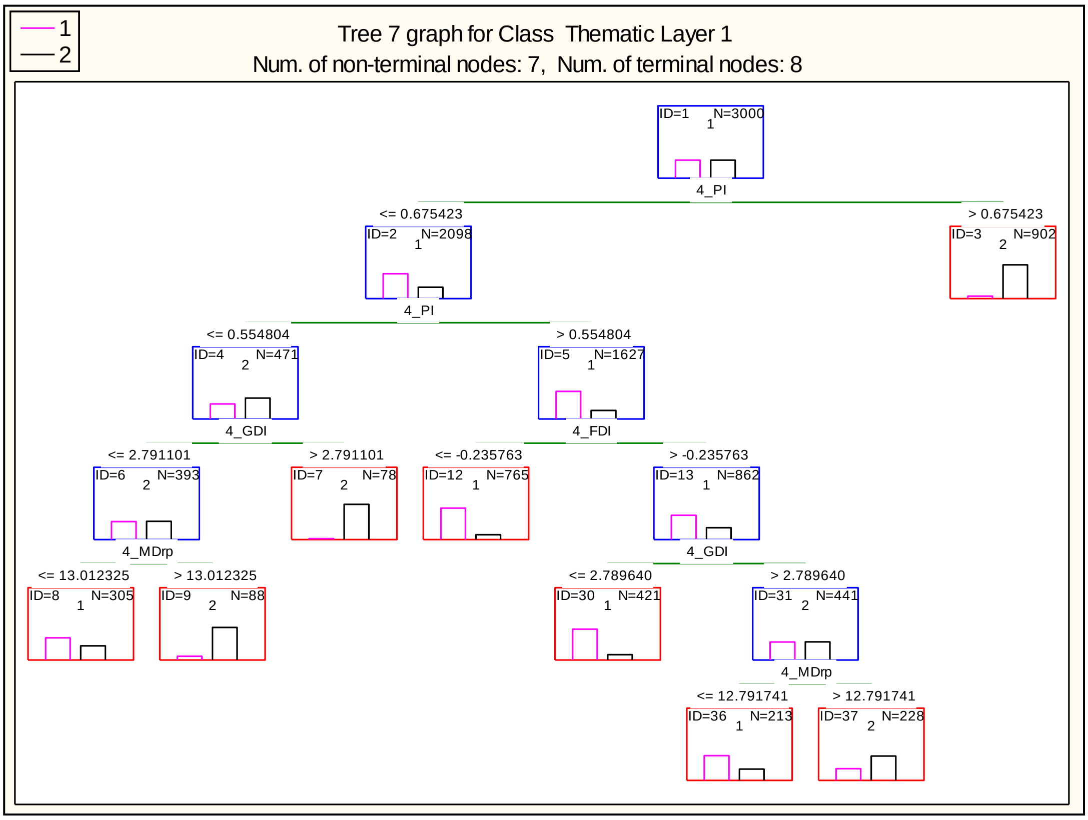

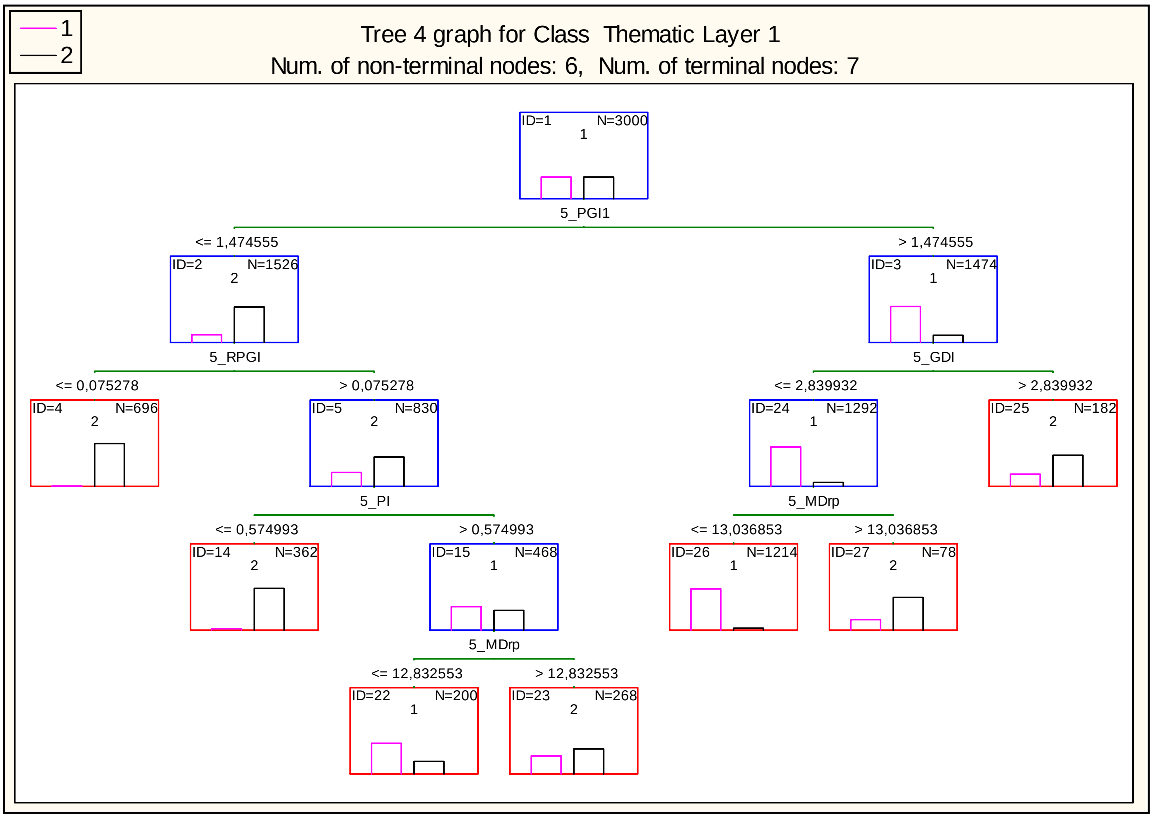

(Fig. 29,30 - 17/4/2020 and 9/5/2020 DT)

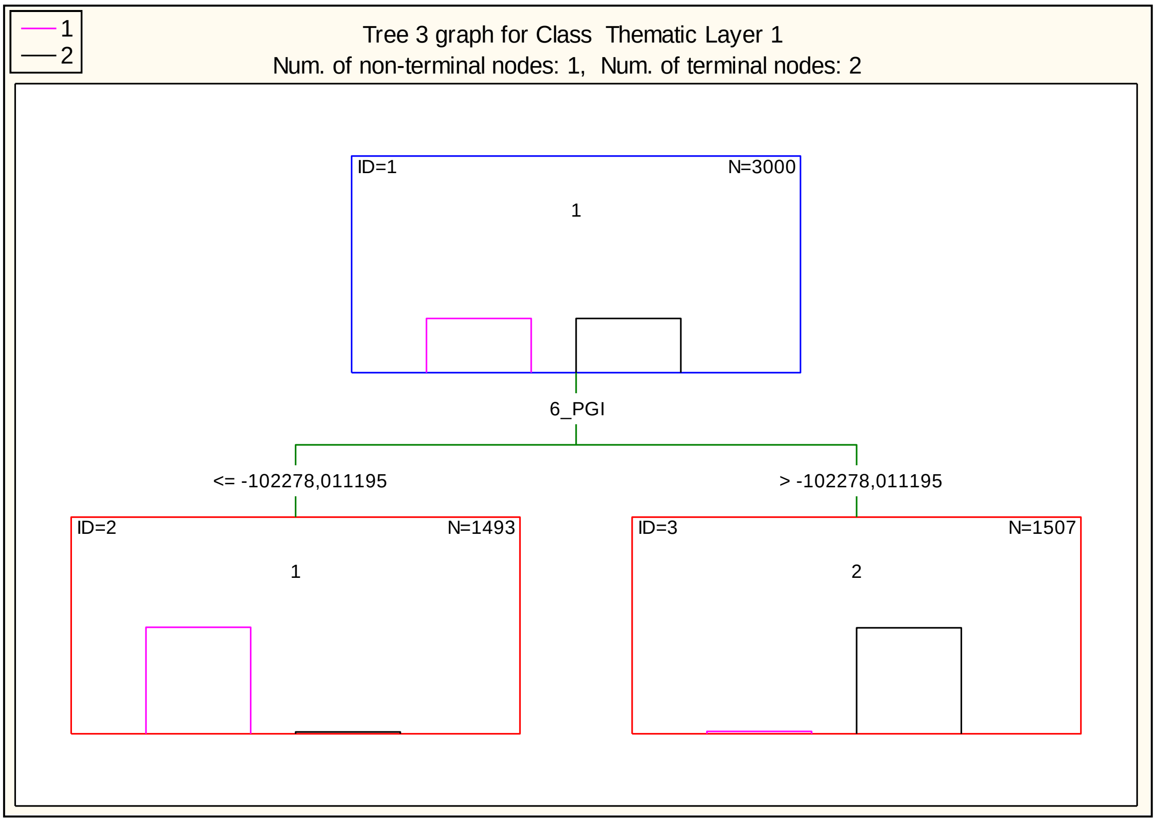

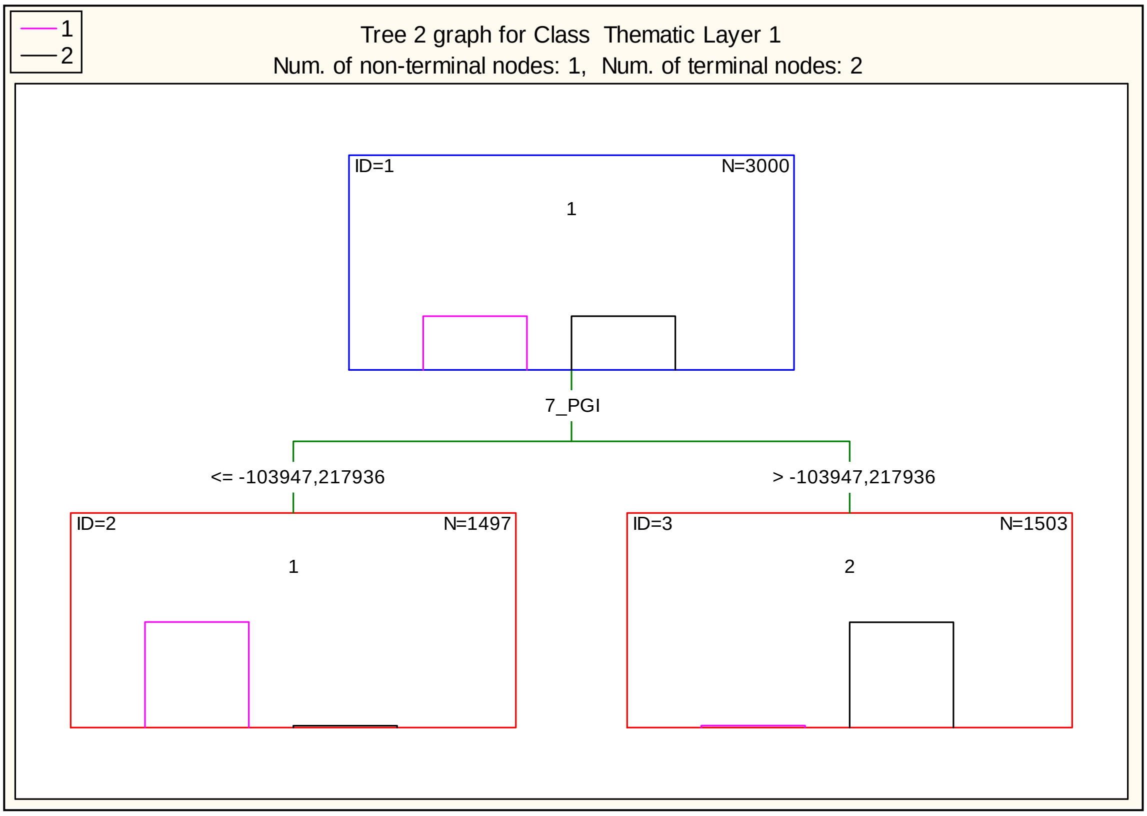

(Fig. 31,32 - 28/6/2020 and 3/7/2020 DT)

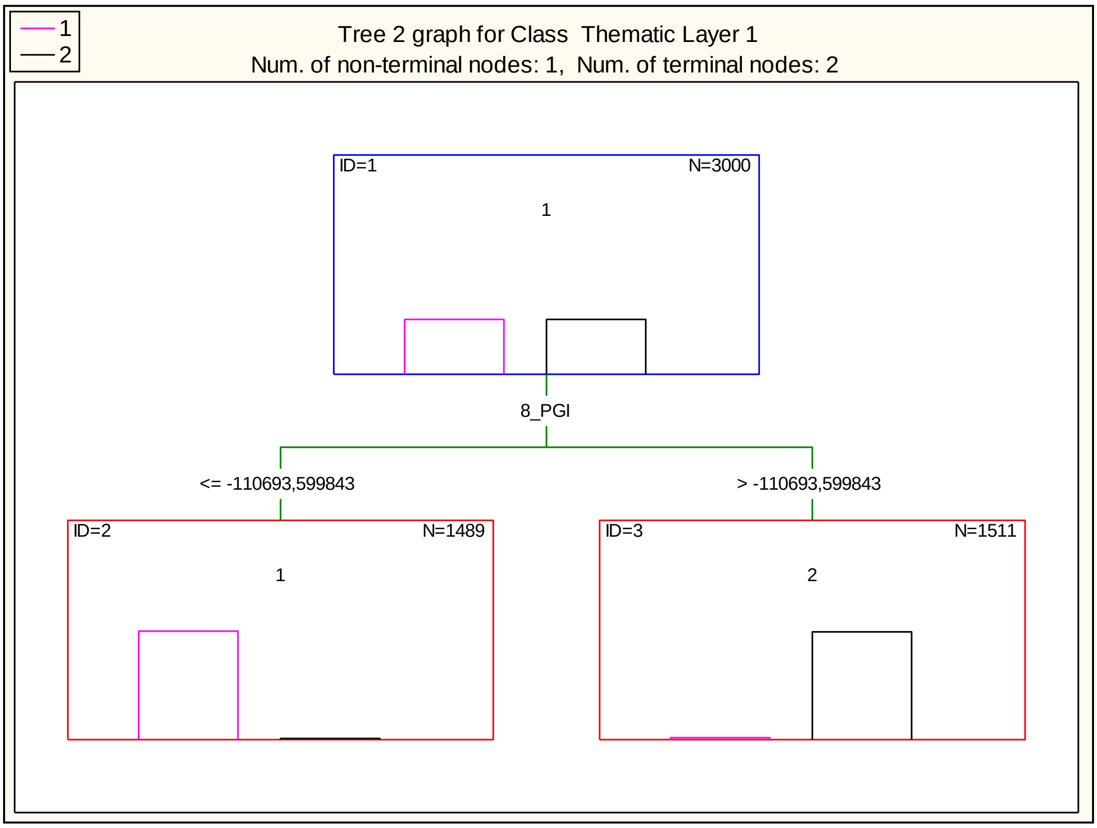

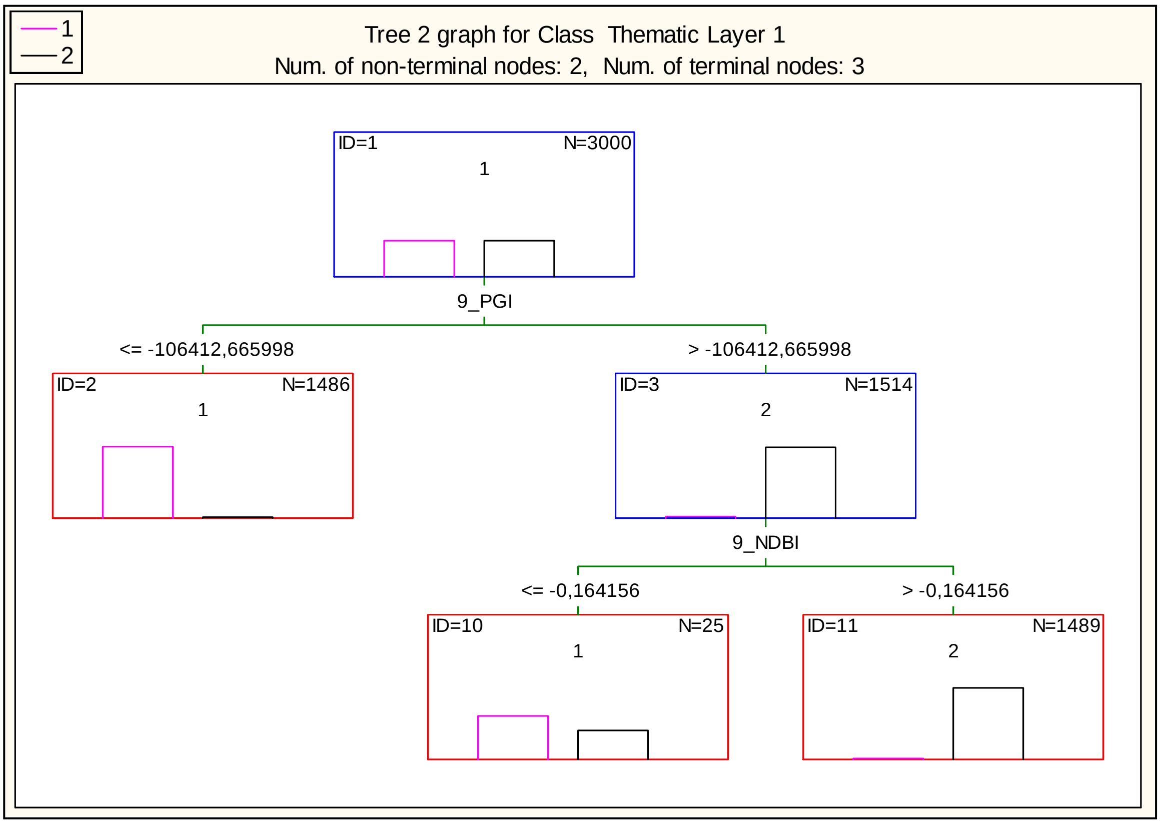

(Fig. 33,34 - 23/7/2020 and 2/8/2020 DT)

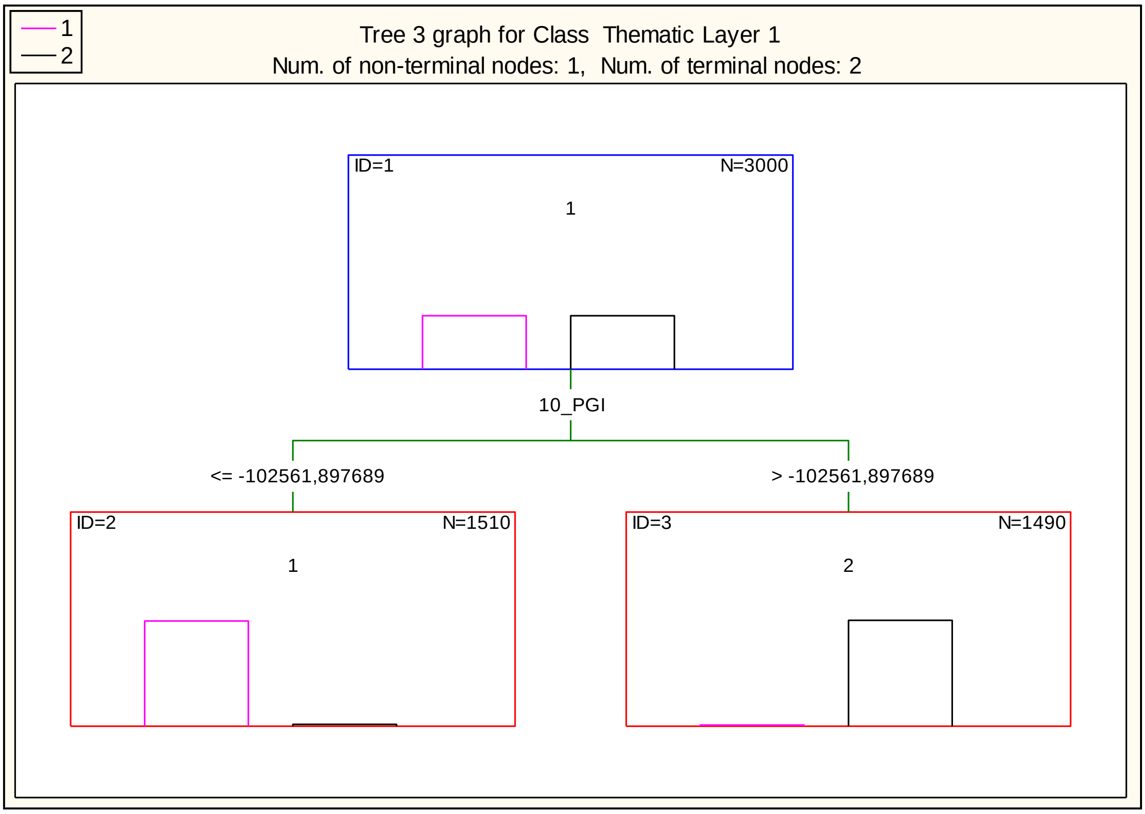

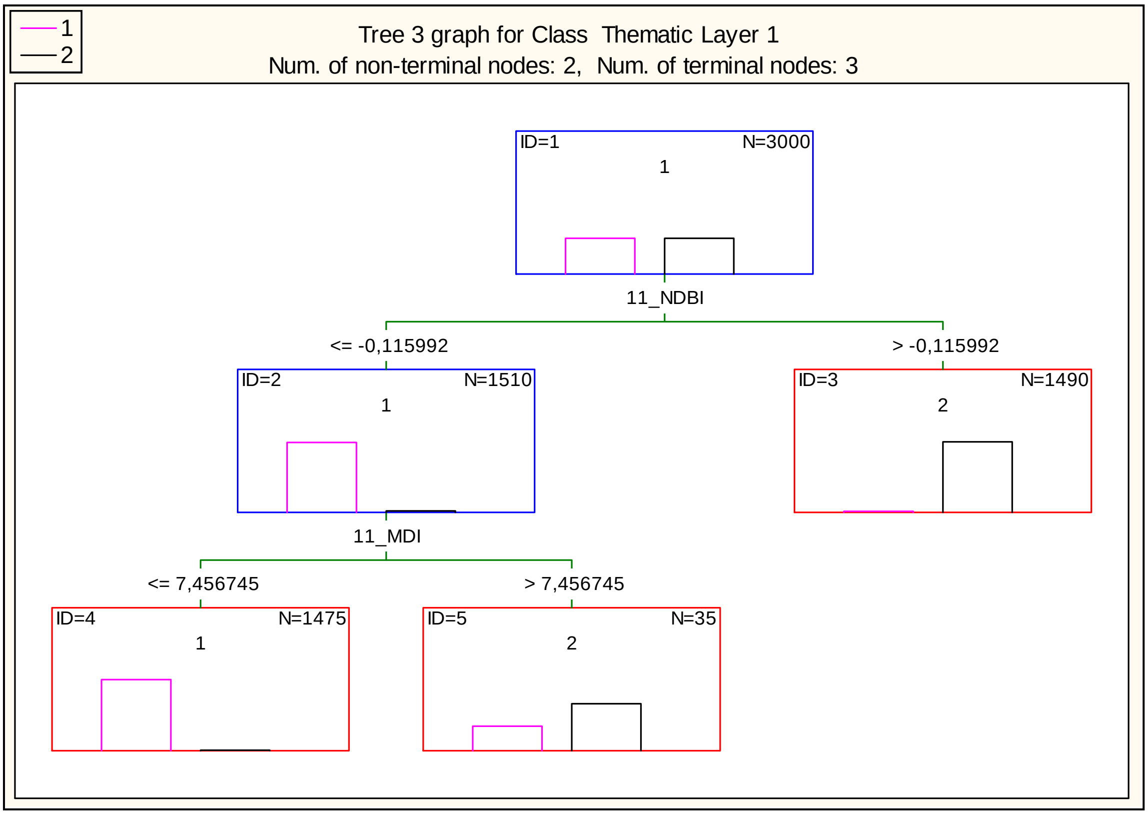

(Fig. 34,35 - 12/8/2020 and 27/8/2020 DT)

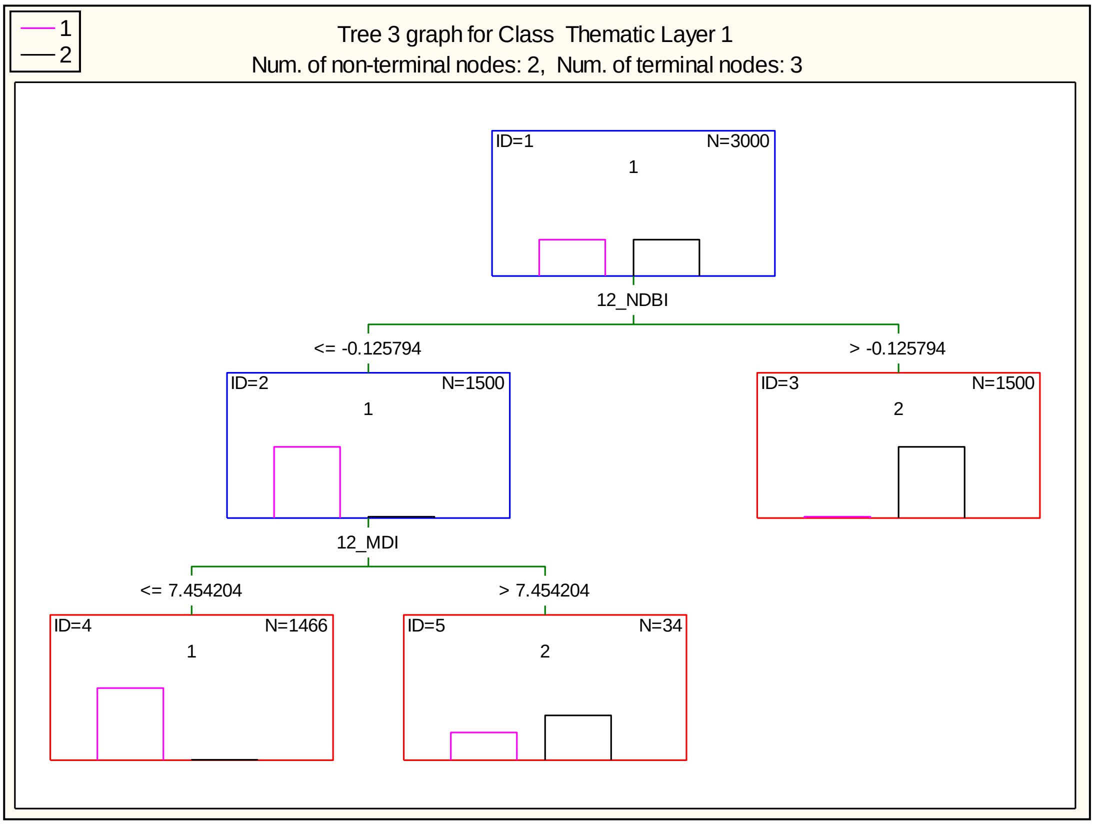

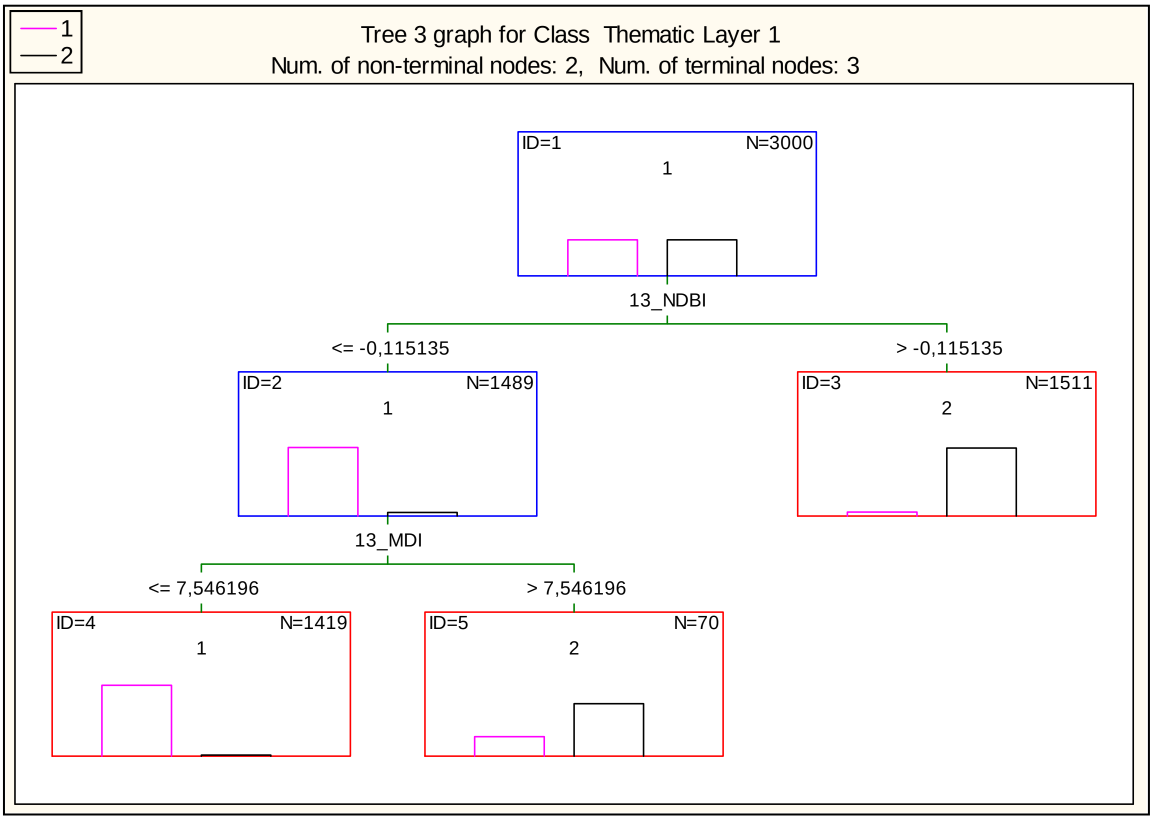

(Fig. 35,36 - 7/9/2020 and 6/10/2020 DT)

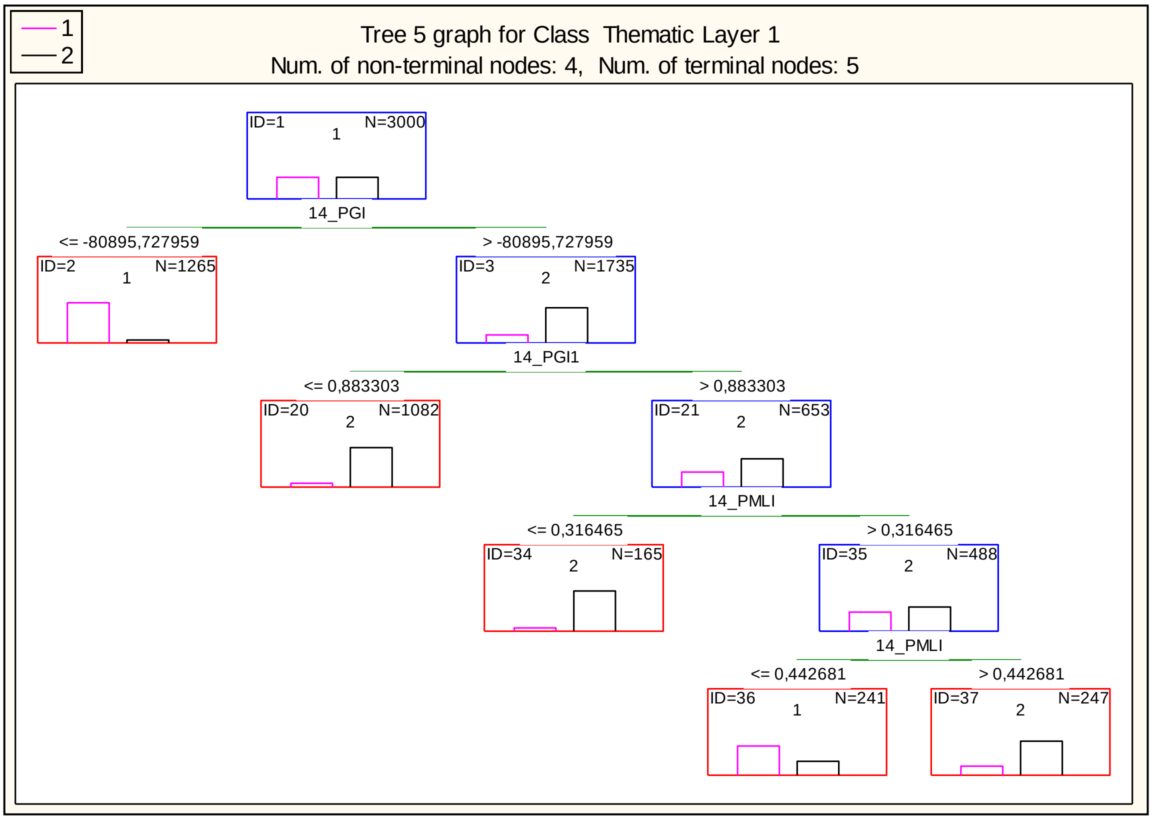

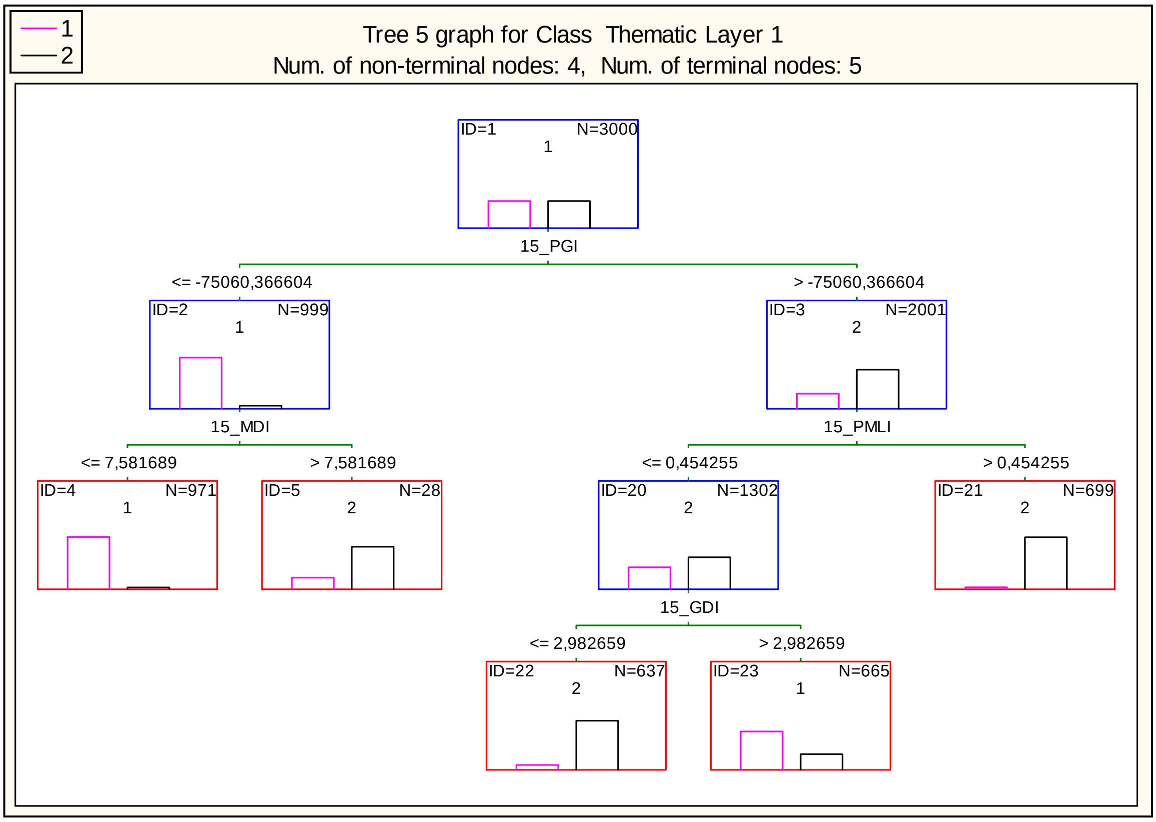

(Fig. 37,38 - 31/10/2020 and 15/11/2020 DT)

2.4.2 Classification accuracy

The evaluation of classification accuracy in this paper was based on two types of error matrices (i.e., error matrix based on 3000 objects and those based on pixels calculated on three manually digitized ground truth zones). Each column of the matrix represents the predicted values, while each row represents the real values. The element on row "i" and column "j" is the number of cases in which the classifier has classified the "true" class i as class j. Through this matrix it is observable if there is "confusion" in the classification of different classes. Through the use of the confusion matrix it is possible to calculate four coefficients:

- The kappa coefficient (K), also known as Cohen's kappa coefficient. It is a concordance index that takes into account the probability of random agreement; the index calculated on the basis of the ratio between the excess agreement with respect to the probability of random agreement and the maximum obtainable excess;
- The overall accuracy (OA) is calculated by summing the number of correctly classified values and dividing by the total number of values. The correctly classified values are located along the upper-left to lower-right diagonal of the confusion matrix. The total number of values is the number of values in either the truth or predicted-value arrays;
- Producer accuracy (PA) is the probability that a value in a given class was classified correctly;
- User accuracy (UA) is the probability that a value predicted to be in a certain class really is that class. The probability is based on the fraction of correctly predicted values to the total number of values predicted to be in a class;

As regards the values of OA and kappa (from Table 11 to Table 25), the accuracies achieved by the single S2 images were relatively low in the first months of the year when there is not much presence of greenhouses, while in the months in which the PGI index is the most significant feature, the results were very good reaching the peak precision in July (OA = 98.63%; KIA = 0.973).

	GH	Non-GH	
GH	1425	75	1500
Non-GH	146	1354	1500
	1571	1429	3000

Overall accuracy	**92,63**	**KIA**	**0,853**
	greenhouse	non-greenhouse	
Producer's accuracy	**95,00**	**90,27**	
User's accuracy	90,71	94,75	

(Table 11 – 25/01/2020 error matrix)

	GH	Non-GH	
GH	1322	178	1500
Non-GH	120	1380	1500
	1442	1558	3000

Overall accuracy	**90,07**	**KIA**	**0,801**
	greenhouse	non-greenhouse	
Producer's accuracy	**88,13**	**92,00**	
User's accuracy	91,68	88,58	

(Table 12 - 9/02/2020 error matrix)

	GH	Non-GH	
GH	1192	308	1500
Non-GH	155	1345	1500
	1347	1653	3000

Overall accuracy	**84,57**	**KIA**	**0,691**
	greenhouse	non-greenhouse	
Producer's accuracy	**79,47**	**89,67**	
User's accuracy	88,49	81,37	

(Table 13 – 13/03/2020 error matrix)

	GH	Non-GH	
GH	1355	145	1500
Non-GH	349	1151	1500
	1704	1296	3000

Overall accuracy	**83,53**	**KIA**	**0,671**
	greenhouse	non-greenhouse	
Producer's accuracy	**90,33**	**76,73**	
User's accuracy	79,52	88,81	

(Table 14 – 17/04/2020 error matrix)

	GH	Non-GH	
GH	1301	199	1500
Non-GH	113	1387	1500
	1414	1586	3000

Overall accuracy	**89,60**	**KIA**	**0,792**
	greenhouse	non-greenhouse	
Producer's accuracy	**86,73**	**92,47**	
User's accuracy	92,01	87,45	

(Table 15 – 9/05/2020)

	GH	Non-GH	
GH	1467	33	1500
Non-GH	26	1474	1500
	1493	1507	3000

Overall accuracy	**98,03**	**KIA**	**0,961**
	greenhouse	non-greenhouse	
Producer's accuracy	**97,80**	**98,27**	
User's accuracy	98,26	97,81	

(Table 16 – 28/06/2020 error matrix)

	GH	Non-GH	
GH	1472	28	1500
Non-GH	25	1475	1500
	1497	1503	3000

Overall accuracy	**98,23**	**KIA**	**0,965**
	greenhouse	non-greenhouse	
Producer's accuracy	**98,13**	**98,33**	
User's accuracy	98,33	98,14	

(Table 17 - 3/07/2020 error matrix)

	GH	Non-GH	
GH	1474	26	1500
Non-GH	15	1485	1500
	1489	1511	3000

Overall accuracy	**98,63**	**KIA**	**0,973**
	greenhouse	non-greenhouse	
Producer's accuracy	**98,27**	**99,00**	
User's accuracy	98,99	98,28	

(Table 18 – 23/07/2020)

	GH	Non-GH	
GH	1482	18	1500
Non-GH	29	1471	1500
	1511	1489	3000

Overall accuracy	**98,43**	**KIA**	**0,969**
	greenhouse	non-greenhouse	
Producer's accuracy	**98,80**	**98,07**	
User's accuracy	98,08	98,79	

(Table 19 – 2/08/2020 error matrix)

	GH	Non-GH	
GH	1483	17	1500
Non-GH	27	1473	1500
	1510	1490	3000

Overall accuracy	**98,53**	**KIA**	**0,971**
	greenhouse	non-greenhouse	
Producer's accuracy	**98,87**	**98,20**	
User's accuracy	98,21	98,86	

(Table 20 – 12/08/2020 error matrix)

	GH	Non-GH	
GH	1466	34	1500
Non-GH	9	1491	1500
	1475	1525	3000

Overall accuracy	**98,57**	**KIA**	**0,971**
	greenhouse	non-greenhouse	
Producer's accuracy	**97,73**	**99,40**	
User's accuracy	99,39	97,77	

(Table 21 – 27/08/2020 error matrix)

	GH	Non-GH	
GH	1457	43	1500
Non-GH	9	1491	1500
	1466	1534	3000

Overall accuracy	**98,27**	**KIA**	**0,965**
	greenhouse	non-greenhouse	
Producer's accuracy	**97,13**	**99,40**	
User's accuracy	99,39	97,20	

(Table 22 – 7/09/2020 error matrix)

	GH	Non-GH	
GH	1397	103	1500
Non-GH	22	1478	1500
	1419	1581	3000

Overall accuracy	**95,83**	**KIA**	**0,917**
	greenhouse	non-greenhouse	
Producer's accuracy	**93,13**	**98,53**	
User's accuracy	98,45	93,49	

(Table 23 – 6/10/2020 error matrix)

	GH	Non-GH	
GH	1340	160	1500
Non-GH	166	1334	1500
	1506	1494	3000

Overall accuracy	**89,13**	**KIA**	**0,783**
	greenhouse	non-greenhouse	
Producer's accuracy	**89,33**	**88,93**	
User's accuracy	88,98	89,29	

(Table 24 – 31/10/2020 error matrix)

	GH	Non-GH	
GH	1409	91	1500
Non-GH	227	1273	1500
	1636	1364	3000

Overall accuracy	**89,40**	**KIA**	**0,788**
	greenhouse	non-greenhouse	
Producer's accuracy	**93,93**	**84,87**	
User's accuracy	86,12	93,33	

(Table 25 – 15/11/2020)

Overall, the error matrix referred to the statistical indices (Table 26) gave excellent results. Among the 1500 objects pre-classified as greenhouses, 1456 greenhouses were well classified while 14 were wrong. Among the 1500 objects classified as Non-GH 1487 were well classified and 13 were wrong. The OA at 99,10% and the K=0,982 are values never reached in previous studies and also the affirmation of the PGI index as in the studies done on Almeria in (Manuel A. Aguilar A. V., 2015), (Manuel A. Aguilar A. N., 2016) can be a very interesting result. Therefore, from very high values of OA and K it was possible to begin to ascertain the robustness of this classification based on the PGI index.

	GH	Non-GH	
GH	1486	14	1500
Non-GH	13	1487	1500
	1499	1501	3000

Overall accuracy	**99,10**	**KIA**	**0,982**
	greenhouse	non-greenhouse	
Producer's accuracy	**99,07**	**99,13**	
User's accuracy	99,13	99,07	

(Table 26 all statistic features error matrix)

2.4.3 Importance of Features

The ranking of the 10 most important characteristics used for image classification is shown in Table 28. The ranking is obtained by combining the importance of the characteristics of all images in the S2 time series. At the top of the most important characteristics ranking there is obviously the SD_PGI as we have already seen in the DT. Next comes the DIF_PIG (importance = 0.994612) and the MIN_PGI (importance = 0.983871). This result further demonstrated how decisive the PGI index is in the classification. In the rankings of importance of the individual Sentinel-2 images, the trend is very similar to that already observed by the decision trees shown above. Therefore in the summer months the PGI value stands out and the NDBI value occasionally.

Feature	**Rank**	**Importance**
SD_PGI	100	1,000000
DIF_PGI	99	0,994612
MIN_PGI	98	0,983871
SD_PGI1	96	0,963691
MAX_PGI1	95	0,945188
DIF_PGI1	94	0,935899
SD_GDI	93	0,928027
DIF_GDI	91	0,913926
MEAN_PGI	91	0,907553
SD_MDI	88	0,880359
MEAN_PGI1	88	0,877719
DIF_MDI	85	0,845005
MEAN_NBDI	81	0,813513
MIN_NBDI	79	0,789848

DIF_PMLI	76	0,760364
MEAN_Vi	71	0,712151
SD_MDLP	70	0,701919
MIN_MDI	69	0,689118
DIF_MDLP	69	0,685976
DIF_NBDI	68	0,682576
MEAN_FDI	68	0,681668
SD_PMLI	68	0,677653
MEAN_MDI	63	0,631106
SD_NBDI	61	0,607550
MIN_GDI	57	0,567284
MAX_MDLP	56	0,563391
MAX_FDI	54	0,544853
MEAN_MDLP	53	0,525674
SD_RPGI	48	0,476495
DIF_NDVI	48	0,475565
DIF_PI	47	0,472385
DIF_RPGI	46	0,463589
SD_Vi	44	0,442238
MIN_Vi	44	0,439512
DIF_Vi	44	0,437763
SD_PI	39	0,389674
SD_NDVI	39	0,387907
MEAN_GDI	38	0,382981
DIF_FDI	38	0,382780
MIN_PMLI	37	0,371398
MEAN_RPGI	33	0,326079

MAX_RPGI	32	0,324860
SD_FDI	32	0,322707
MEAN_MDRP	26	0,255436
MIN_NDVI	25	0,254720
MIN_PI	25	0,253019
MAX_PI	24	0,243945
MEAN_PMLI	24	0,243025
MAX_NDVI	24	0,237738
MAX_MDRP	24	0,235344
MEAN_PI	23	0,226884
MEAN_NDVI	22	0,223888
MAX_GDI	21	0,211141
MAX_PMLI	21	0,207191
MIN_RPGI	21	0,207092
MAX_Vi	20	0,203978
DIF_MDRP	16	0,164264
MAX_PGI	13	0,133146
SD_MDRP	11	0,107086
MAX_NBDI	10	0,101944
MIN_MDRP	7	0,068849
MIN_PGI1	5	0,053814
MAX_MDI	4	0,038258
MIN_MDLP	3	0,026483
MIN_FDI	1	0,011235

(Table 27 – Importance ranking)

2.4.4 Pixel-based accuracy

After analyzing the most relevant characteristics and the most stable cutting values over time, the next step was to consolidate the result obtained until now by making a new classification following the decision rule corresponding to the DT. The selected feature was obviously the SD_PGI derived from the S2 time series (Fig. 25). This procedure was again implemented in eCognition to perform pixel-based accuracy assessment. Once the classification was done on eCognition, the goal was to create 3 Ground Truth zone masks manually digitized. The 3 sub-zones (Fig. 39, 40, 41) were chosen based on the density and distribution of greenhouses present within them. Ground truth is the information or data collected on the site so that the input data (image) can be related to the actual characteristics and is considered very correct and appropriate with respect to the input characteristics. This process compares the pixel on a satellite image with what is present in reality (at the moment) in order to verify the content of the pixel on the image. In addition, the commission error and omission for the accuracy assessment can be calculated in the same way as the OBIA approach.

(Fig. 39,40,41 – Zone 1 coordinates UTM cornes: Upper-Left: 662000 m, 4546000 m Bottom-Right: 664000 m, 4544000 m; Zone 2 coordinates UTM corners: Upper-Left: 662000 m, 4540000 m Bottom-Right: 664000 m, 4538000 m; Zone 3 coordinates UTM corners: Upper-Left: 658000 m, 4540000 m Bottom-Right: 660000 m, 4538000 m)

the digitized masks were rasterized in TIF assigning to each pixel the values of 1 and 2 (respectively corresponding to GH and Non-GH). The pixels of the TIFs of the 3 sub-zones were compared with OBIA classification obtained from the DT. From this comparison 3 new dispersion matrixes were calculated (one for each zone) similar to those made previously but referring to the pixels instead of the objects. Each pixel has an area of 1x1 m (because the digitization was made from the Deimos-2 image which has a geometric resolution of 1 m) and the sub-zones considered are squares with a side of 2 km. Therefore each sub-zone contains 4000000 pixels classified and compared with the OBIA classification.

2.4.5 Comparison procedure

New eCognition files have been created for each Ground Truth zone. The input data is the same as the previous classification except for the thematic layer. In this case the vector file used does not contain the binary pre-classification (GH or Non-Gh) but all the characteristics and statistical indices, calculated in the previous steps, have been integrated into its attribute table. Therefore, once the input data has been entered, a new classification has been created in the following way. A new "assign class" has been added in which all segments of the layer with SD_PGI value greater than 21153,591680 are classified as greenhouses. Conversely, another class has been added in which all segments with SD_PGI values less than 21153.591680 are classified as Non-Gh.

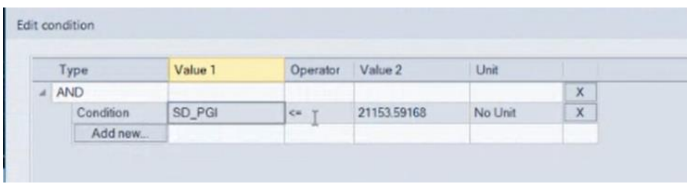

(Fig. 42 - Example classification based on SD_PGI in eCognition)

In the Figure 43 it is possible to notice the new classification based on SD_PGI compared with the previous one (1500 GH Objects).

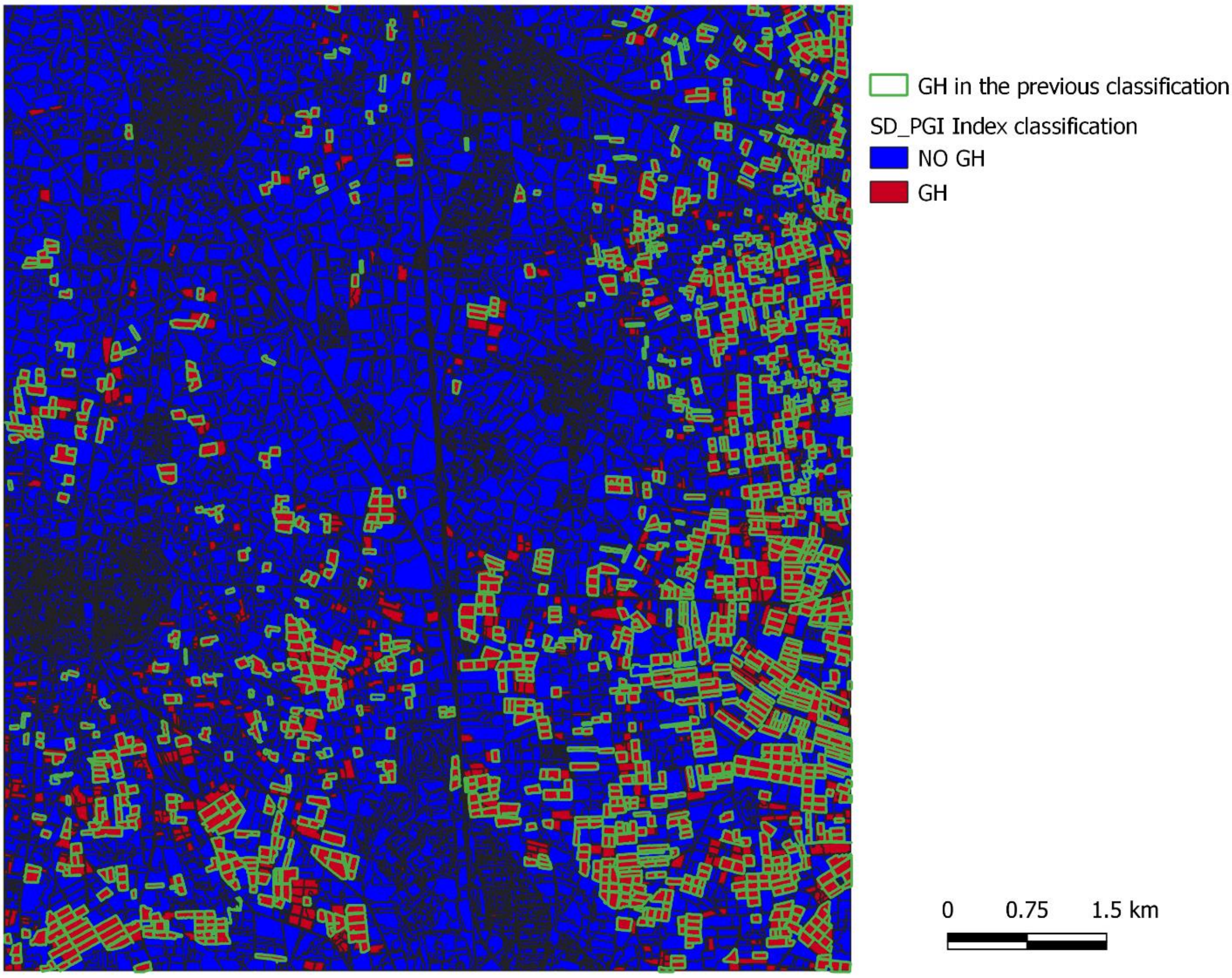

(Fig. 43 – New classification with SD_PGI)

At this point the masks have been inserted into the software. The procedure was done individually for the 3 sub-zones. In order to insert the mask, eCognition needs two types of input files:

- The TIF file with the pixels classified as 1 -> Gh E 2 -> Non-Gh;

- An excell table with 4 columns. In the first column there is the ID of the pixels (1 or 2), in the second, third and fourth column there is the RGB combination and in the last there is the name of the class;

ID	Red	Green	Blue	Class_Names
1	255	0	0	GH
2	0	0	255	Non_GH

(Table 28 - Input table for the mask)

The TIF was created using GIS, transforming the layers (Fig. 44, 45, 46) of all the greenhouses into raster (Fig. 47, 48, 49). In the transformation the "class" was used as the field value and the pixel measurement was set equal to 1 as previously mentioned.

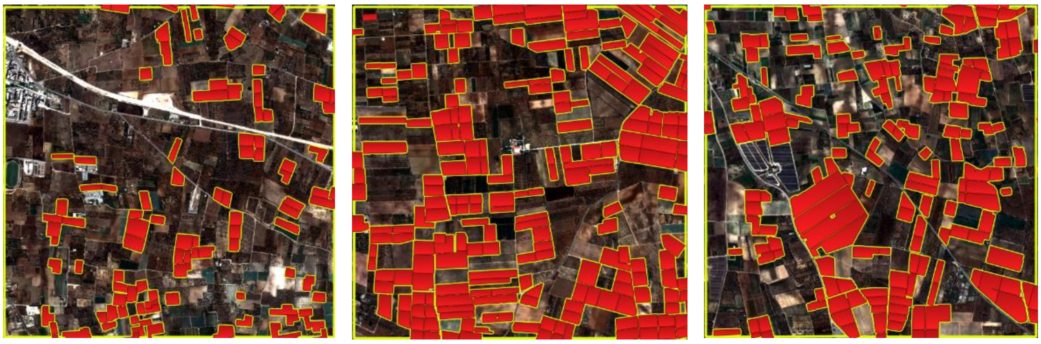

(Fig. 44,45,46 – GH layers for each sub-zone)

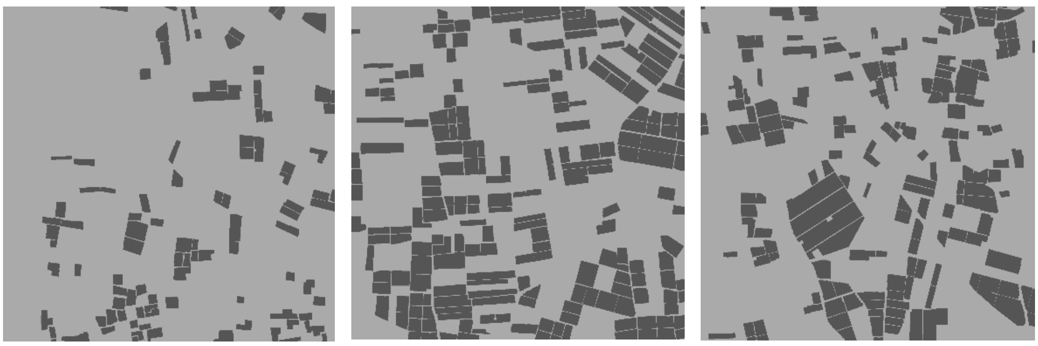

(Fig. 47, 48, 49 – TIF masks)

After the two types of input file described above have been loaded, the created masks appear on the eCognition software (Fig. 50, 51, 52). By zooming into one of the 3 masks, divergences between the two types of classification have already been noted. it is evident that there are segments of the thematic layer in which inside there are pixels of different classification.

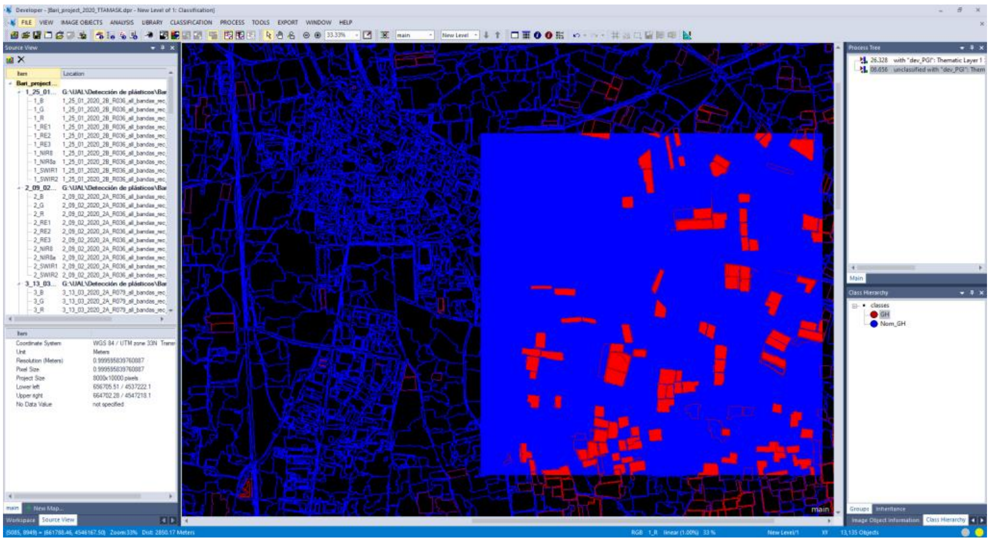

(Fig. 50 – eCognition mask zone 1)

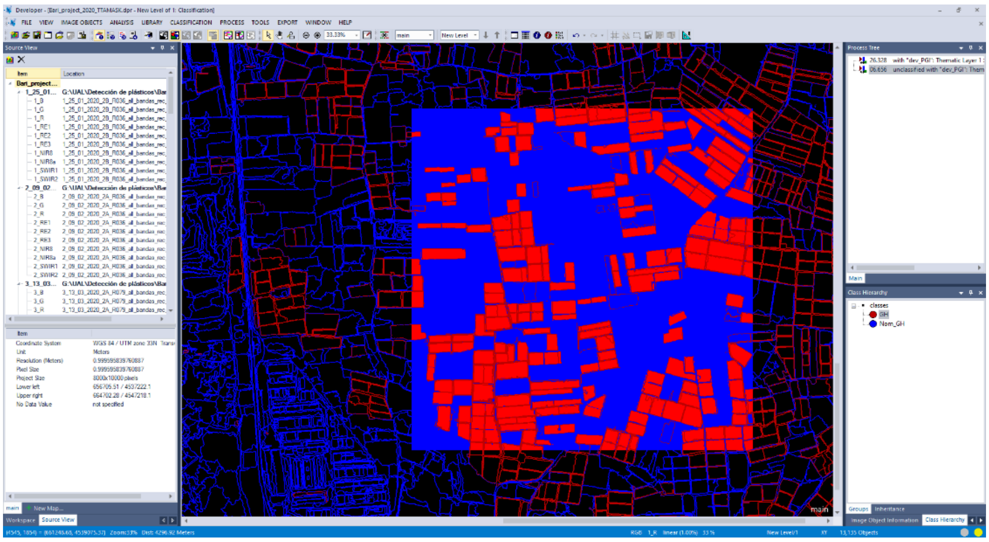

(Fig. 51 – eCognition mask zone 2)

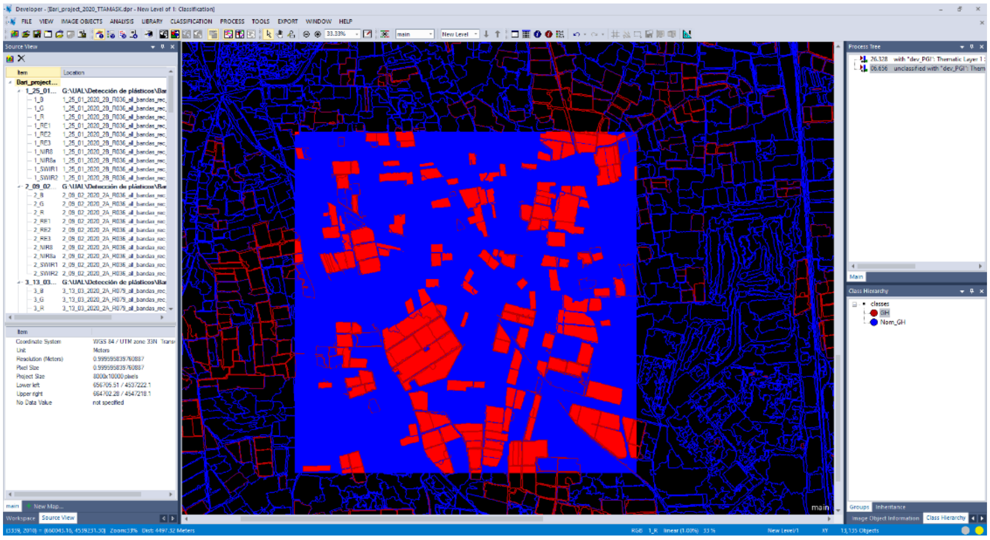

(Fig. 52 – eCognition mask zone 3)

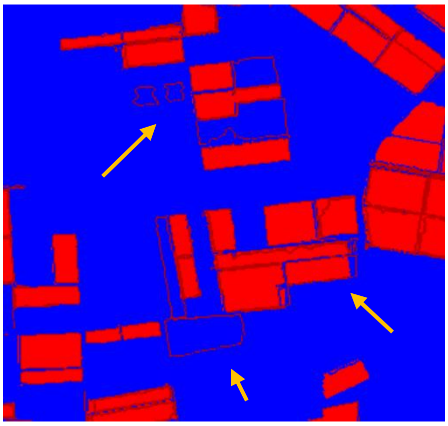

(Fig. 53 - example misclassification)

This led to values of "OA" and "K", for the respective three areas analyzed, lower than those calculated in the OBIA classification made previously. In fact, the new error matrix for each mask was calculated and the following values were obtained:

TTAMASK ZONE 1BARI

	GH	Non-GH	
GH	428083	117737	545820
Non-GH	21037	3437144	3458181
	449120	3554881	4004001

Overall accuracy	**96,53**	**KIA**	**0,841**
	greenhouse	non-greenhouse	
Producer's accuracy	**78,43**	**99,39**	
User's accuracy	95,32	96,69	

(Table 29 – error matrix zone 1)

TTAMASK ZONE 2 BARI

	GH	Non-GH	
GH	1388482	283268	1671750
Non-GH	67661	2266591	2334252
	1456143	2549859	4006002

Overall accuracy	**91,24**	**KIA**	**0,817**
	greenhouse	non-greenhouse	
Producer's accuracy	**83,06**	**97,10**	
User's accuracy	95,35	88,89	

(Table 30 error matrix zone 2)

TTAMASK ZONE 3 BARI

	GH	Non-GH	
GH	951350	245350	1196700
Non-GH	133260	2676042	2809302
	1084610	2921392	4006002

Overall accuracy	**90,55**	**KIA**	**0,768**
	greenhouse	non-greenhouse	
Producer's accuracy	**79,50**	**95,26**	
User's accuracy	87,71	91,60	

(Table 31 error matrix zone 3)

The accuracy values are obviously lower than the OBIA classification but are still high enough to confirm the robustness of the SD_PGI parameter in the classification of greenhouses in the area under study.

3 Conclusions

In this work, an approach similar to that made in previous publications was presented to address the problem of mapping greenhouses but with a different type of starting images. A greater verification of the accuracy of the classification and above all an area was studied (Bari) containing a typology and a temporal distribution of greenhouses different from those studied in previous studies such as Almeria. The workflow carried out for the classification with the OBIA approach was based on the Sentinel-2 and Deimos-2 data pair, which until now had never been used for this type of task in the Bari area. The first phase focused on achieving the optimal segmentation for the individual greenhouses using the MRS algorithm on the single Deimos-2 orthoimage. The use of the free access control tool called AssesSeg allowed to find an ED with excellent relationship with the visual quality of the greenhouse segmentations, allowing to select the main MRS parameters (i.e., Scale, Shape and Compactness) for the orthoimage. It is worth mentioning that the AssesSeg tool can work with segmentation algorithms other than MRS. Therefore, segmentation evaluation is not strictly dependent on the use of eCognition. The next step was to do binary preclassification of the previously segmented objects into GH or Non-GH. The DT classifier was applied to determine the best statistical seasonal characteristics (MEAN, MAX, MIN, DIF, SD) derived from different groups of indices based on a single object (spectral, vegetation indices and plastic detection indices). The individual object-based features have been extracted from every single pre-processed S2 scene. The standard deviation of the Plastic Greenhouse Index (SD (PGI)) was the most important statistical seasonal characteristic for the time series. This result is of considerable importance because it is the same obtained by the DT in the publication of (Abderrahim Nemmaoui, 2018) for the Almeria site. Although the greenhouses of Almeria are different both from the structural point of view and, regarding to the crops present inside, this work has brought great confirmation about the robustness of this statistical data for the classification of greenhouses. Also from a temporal point of view, the PGI index reported by (Dedi Yang, 2017) proved to be the most exceptional following the seasonal trend of the presence of greenhouses in the Bari area with good results. The OA and kappa accuracy values for binary classification obtained from S2A DT (OA = 99.10%; Kappa = 0.8982) give further confirmation on the use of the Sentinel time series as has already been demonstrated by Nemmaoui et al. (2018). Furthermore, in the pixel-based verification of the classification, despite the values of OA and K are lower for obvious reasons, however, they have values high enough to confirm the robustness of the data. In conclusion, overall, the proposed workflow was successfully demonstrated using Deimos-2 and Sentinel-2 satellite images, demonstrating that the S2 time series produced slightly better accuracies than L8 used in previous publications, mainly in the binary pre-classification phase. However, more work is needed to learn much more about the influence on crop classification under PCG of several factors such as crop varieties, type, age and thickness of the plastic cover, and the geometry of the greenhouse roof.

References

Abderrahim Nemmaoui, M. A. (2018). Greenhouse Crop Identification from Multi-Temporal Multi-Sensor Satellite Imagery Using Object-Based Approach: A Case Study from Almería (Spain). *MDPI*.

Antonio Novelli, M. A. (2016). Performance evaluation of object based greenhouse detection fromSentinel-2 MSI and Landsat 8 OLI data: A case study from Almería(Spain). *ELSEVIER*.

Breiman, L., Friedman, J., Olshen, R., & Stone, C. (s.d.). Classification and Regression Trees. *Chapman & Hall/CRCPress: Boca Raton*, 1984.

D. Marceau, T. B. (2003). A multi-scale segmentation/object relationship modelling methodology for landscape analysis. *Ecological Modelling*, 233-249.

Dedi Yang, J. C. (2017). Mapping plastic greenhouse with medium spatial resolution satellite data: Development of a new spectral index. *ELSEVIER*.

Kyriacos Themistocleous, C. P. (2020). Investigating Detection of Floating Plastic Litter from Space Using Sentinel-2 Imagery. *MDPI*.

Lauren Biermann, D. C.-V. (2020). Finding Plastic Patches in Coastal Waters using Optical Satellite Data. *www.nature.com/scientificreports*.

Luigi Tarricone, F. T. (2021). Uva da tavola e coperture: rischi e peculiarità. *Uva da tavola*.

Manuel A. Aguilar, A. N. (2016). Object-Based Greenhouse Mapping Using Very High Resolution Satellite Data and Landsat 8 Time Series. *MDPI*.

Manuel A. Aguilar, A. V. (2015). Object-Based Greenhouse Horticultural Crop Identification from Multi-Temporal Satellite Imagery: A Case Study in Almeria, Spain. *www.mdpi.com/journal/remotesensing*.

Manuel Ángel Aguilar, R. J.-L.-S. (2020). Evaluation of the Consistency of Simultaneously Acquired Sentinel-2 and Landsat 8 Imagery on Plastic Covered Greenhouses. *MDPI*.

Marceau, D. (1999). The scale issue in the social and natural sciences. *Canadian Journal of Remote Sensing*.

Methodological proposal to assess plastic greenhouses land cover change from the combination of archival aerial orthoimages and Landsat data. (2018). *Biosystems Engineering, ScienceDirect*.

Navulur, K. (2007). Multispectral image analysis using the object-oriented paradigm.

Oscar Gonzalez-Yebra, M. A. (2018). Methodological proposal to assess plastic greenhouses land cover change from the combination of archival aerial orthoimages and Landsat data. *ScienceDirect, Biosystem Engineerring*.

R. Kettig, D. L. (1976). Classification of multispectral image data by extraction and classification of homogeneous objects.

R. Kettig, D. L. (2008). Deforestation in Central Africa: Estimates at regional, national and landscape levels by advanced processing of systematically-distributed Landsat extracts.

R. Kettig, D. L. (2009). Object-oriented change detection for the city of Harare, Zimbabwe.

T. Blaschke, S. L. (2000). Object-oriented image processing in an integrated GIS/remote sensing environment and perspectives for environmental applications.

U.C. Benz, P. H. (2004). Multi-resolution, object-oriented fuzzy analysis of remote sensing data for GIS-ready information.

Zambon, M., Lawrence, R., Bunn, A., & Powell, S. (2006). Effect of alternative splitting rules on image processing using classification tree analysis.

[TITOLO DEL DOCUMENTO]